REPORT DOCUMENTATION PAGE

Form Approved OMB NO. 0704-0188

1. REPORT DATE (DD-MM-YYYY)	2. REPORT TYPE	3. DATES COVERED (From - To)
06-11-2019	Final Report	24-Aug-2015 - 23-Jan-2019

4. TITLE AND SUBTITLE
Final Report: Nonlocal and Fractional Order Methods for Near-wall Turbulence, Large-eddy Simulation, and Fluid-structure Interaction

5a. CONTRACT NUMBER
W911NF-15-1-0552

5b. GRANT NUMBER

5c. PROGRAM ELEMENT NUMBER
611102

6. AUTHORS

5d. PROJECT NUMBER

5e. TASK NUMBER

5f. WORK UNIT NUMBER

7. PERFORMING ORGANIZATION NAMES AND ADDRESSES
University of Texas at Austin
101 East 27th Street
Suite 5.300
Austin, TX 78712 -1532

8. PERFORMING ORGANIZATION REPORT NUMBER

9. SPONSORING/MONITORING AGENCY NAME(S) AND ADDRESS (ES)
U.S. Army Research Office
P.O. Box 12211
Research Triangle Park, NC 27709-2211

10. SPONSOR/MONITOR'S ACRONYM(S)
ARO

11. SPONSOR/MONITOR'S REPORT NUMBER(S)
67478-MA.1

12. DISTRIBUTION AVAILIBILITY STATEMENT
Approved for public release; distribution is unlimited.

13. SUPPLEMENTARY NOTES
The views, opinions and/or findings contained in this report are those of the author(s) and should not contrued as an official Department of the Army position, policy or decision, unless so designated by other documentation.

14. ABSTRACT

15. SUBJECT TERMS

16. SECURITY CLASSIFICATION OF:			17. LIMITATION OF ABSTRACT	15. NUMBER OF PAGES	19a. NAME OF RESPONSIBLE PERSON
a. REPORT	b. ABSTRACT	c. THIS PAGE			John Foster
UU	UU	UU	UU		19b. TELEPHONE NUMBER 512-471-6982

RPPR Final Report
as of 07-Nov-2019

Agency Code:

Proposal Number: 67478MA **Agreement Number: W911NF-15-1-0552**
INVESTIGATOR(S):

Name: John T. Foster
Email: jfoster@austin.utexas.edu
Phone Number: 5124716982
Principal: Y

Organization: **University of Texas at Austin**
Address: 101 East 27th Street, Austin, TX 787121532
Country: USA
DUNS Number: 170230239 EIN: 746000203
Report Date: 23-Apr-2019 Date Received: 06-Nov-2019
Final Report for Period Beginning 24-Aug-2015 and Ending 23-Jan-2019
Title: Nonlocal and Fractional Order Methods for Near-wall Turbulence, Large-eddy Simulation, and Fluid-structure Interaction
Begin Performance Period: 24-Aug-2015 **End Performance Period:** 23-Jan-2019
Report Term: 0-Other
Submitted By: John Foster Email: jfoster@austin.utexas.edu
Phone: (512) 471-6982
Distribution Statement: 1-Approved for public release; distribution is unlimited.

STEM Degrees: 1 **STEM Participants:** 1

Major Goals: To seek out, analyze, develop and implement verified solution techniques, along with validation for engineering applications of fractional calculus and other nonlocal methods as applied to computational fluid dynamics (CFD).

Accomplishments: See attached report

Training Opportunities: Nothing to Report

Results Dissemination: “A model for the transport of miscible fluids in the presence of anamalous diffusion.” (with R. Tabasi). ASME 2017 International Mechanical Engineering Congress and Exposition. November 2017.

"A model for the transport of miscible fluids in the presence of anomalous diffusion.” (with R. Tabasi). USACM Thematic Workshop on Isogeometric Analysis and Meshfree Methods. October 2016.

“A model for the transport of miscible fluids in the presence of anomalous diffusion.” (student delivered by R. Tabasi). SIAM CSE. March 2, 2017.

Honors and Awards: Nothing to Report

Protocol Activity Status:

Technology Transfer: Nothing to Report

PARTICIPANTS:

Participant Type: PD/PI
Participant: John Timothy Foster Jr
Person Months Worked: 1.00 **Funding Support:**
Project Contribution:
International Collaboration:
International Travel:
National Academy Member: N

Other Collaborators:

Participant Type: Graduate Student (research assistant)
Participant: Rambod Tabasi
Person Months Worked: 12.00 **Funding Support:**
Project Contribution:
International Collaboration:
International Travel:
National Academy Member: N
Other Collaborators:

ARO GRANT #W911NF-15-1-0552
FINAL REPORT

On nonlocal transport phenomenon

Principal Investigator: John T. Foster, Ph.D., P.E.
The University of Texas at Austin
Institute for Computational Engineering and Sciences
201 E. 24th Street, Stop C0200
Austin, TX 787120027
Phone: 5124716972
E-mail: jfoster@austin.utexas.edu

Submitted to:
Dr. Joseph Myers and Dr. Matt Munson
U.S. Army Research Office
4300 S. Miami Blvd.
Durham, NC 27703-9142

November 4, 2019

EXECUTIVE SUMMARY

Fractional-order operators such as the space-fractional advection-diffusion equation, or special cases of it like the space-fractional Laplacian, have seen considerable treatment in the mathematical literature as specialized techniques for handling microstructural heterogeneity whereby the underlying processes deviate from exponential distribution statistics. As an example, a "heavy tailed" distribution of tracer particle mean squared distances can lead to interesting processes such as Lévy flights. Time-fractional models have also received considerable attention and have found usefulness in modeling history-dependent materials and processes, e.g. viscoelasticity. If we correctly interpret the fractional derivative operation as a nonlocal operator, we can elucidate connections with weakly nonlocal higher-order gradient-based methods, strong (i.e. integral) nonlocal diffusion, and peridynamic mechanics. While fractional order methods have a niche audience in the literature, and they provide the tools to incorporate more general physics, they have yet to find widespread adoption in engineering analysis. The reason for this may partly be due to to the specialized mathematics behind them, but more practical issues arise that are associated with the solution of fractional order equations.

Presented in this report is a collection of mathematical formulations, engineering applications, and a description of numerical solutions to nonlocal equations involved in fluid and heat transport. In the first section we show the connection of a more general class of nonlocal operators to fractional derivative operators, after which we dispense with unnecessary definitions of fractional derivatives (as they are simply special cases of the more general theory) and carry the work forward in this framework to investigate nonlocal advection-diffusion and its role in mixing as well as a nonlocal heat transport model that is used as an upscaling of molecular dynamics to model anomalous transport in a multiphase fluid. Mathematical models and their limiting behavior with respect to their local analogues are presented along with numerical solutions and comparison to experimental results from literature for these applications.

Contents

Introduction

Background

The goal of the research presented herein was to seek out, analyze, develop and implement verified solution techniques, along with validation for *engineering applications* of fractional calculus and other nonlocal methods as applied to computational fluid dynamics (CFD) with a goal of bringing these generalizations of continuum mechanics to a level-of-acceptance equivalent with the classical theories. The specific aims of the research represented challenging problems for establishing sound mathematical approaches and developing unified nonlocal theories and computational tools capable of predicting the responses to fluid and heat transport problems where the separation-of-length scales homogenization assumptions are invalid.

Fractional-order operators such as the space-fractional advection-diffusion equation, or special cases of it like the space-fractional Laplacian, have seen considerable treatment in the mathematical literature as specialized techniques for handling microstructural heterogeneity whereby the underlying processes deviate from exponential distribution statistics. As an example, a "heavy tailed" distribution of tracer particle mean squared distances can lead to interesting processes such as Lévy flights. Time-fractional models have also received considerable attention and have found usefulness in modeling history-dependent materials and processes, e.g. viscoelasticity. If we correctly interpret the fractional derivative operation as a nonlocal operator, we can elucidate connections with weakly nonlocal higher-order gradient-based methods, strong (i.e. integral) nonlocal diffusion, and peridynamic mechanics.

While fractional order methods have a niche audience in the literature, and they provide the tools to incorporate more general physics, they have yet to find widespread adoption in engineering analysis. The reason for this may partly be due to to the specialized mathematics behind them, but more practical issues arise that are associated with the solution of fractional order equations. Popular solution methods are the Grünwald fractional difference quotient, exploiting the fractional derivative as a convolution of an integer-order derivative with a kernel, Fourier and Laplace transform techniques, among others. The most useful of these for numerical computation is the Grünwald fractional difference quotient; however, sharing a similarity with finite difference methods, it's unclear how it can be applied on unstructured data. Additionally, the fractional order methods result in dense tangent matrices requiring considerable computational expense, as well as possible difficulty in the treatment of boundary conditions.

Presented in this report is a collection of mathematical formulations, engineering applications,

and a description of numerical solutions to nonlocal equations involved in fluid and heat transport. In the first section we show the connection of a more general class of nonlocal operators to fractional derivative operators, after which we dispense with unnecessary definitions of fractional derivatives (as they are simply special cases of the more general theory) and carry the work forward in this framework to investigate nonlocal advection-diffusion and its role in mixing as well as a nonlocal heat transport model that is used as an upscaling of molecular dynamics to model anomalous transport in a multiphase fluid. Mathematical models and their limiting behavior with respect to their local analogues are presented along with numerical solutions and comparison to experimental results from literature for these applications.

The remainder of this report is organized as follows: the rest of this chapter demonstrates that fractional differential operators are special cases of more general nonlocal operators. This is demonstrated in the context of the fractional Laplacian and a fractional elasticity model taken from literature. Chapter 2 presents an engineering application of advection-diffusion and viscous fingering in a nonlocal setting. Chapter 3 demonstates a nonlocal homogenization procedure for upscaling molecular dynamics simulations.

Nonlocal Incompressible Navier–Stokes Equations

To briefly demonstrate the idea that fractional derivative models are special cases of more general nonlocal operaters (and provide a well known engineering setting), we'll propose the following nonlocal form of the Navier–Stokes equations (NLNS) for incompressible flow (explicit functional dependence on t is implied but has been dropped for brevity in the notation)

$$\begin{aligned}\frac{\partial u_i(\mathbf{x})}{\partial t} &+ u_j(\mathbf{x}) \int_{\mathcal{H}} \gamma\, \omega(\|\boldsymbol{\xi}\|)\, (u_i(\mathbf{x}') - u_i(\mathbf{x}))\, \frac{\xi_j}{\|\boldsymbol{\xi}\|^2} \mathrm{d}V_\xi \\ &- \int_{\mathcal{H}} \beta\, \omega(\|\boldsymbol{\xi}\|) \frac{\xi_i \left(\underline{\nu}(\mathbf{x}, \mathbf{x}') + \underline{\nu}(\mathbf{x}', \mathbf{x})\right) \xi_j}{\|\boldsymbol{\xi}\|^2} (u_j(\mathbf{x}') - u_j(\mathbf{x})) \mathrm{d}V_\xi \\ &= -\frac{1}{\rho_o} \int_{\mathcal{H}} \gamma\, \omega(\|\boldsymbol{\xi}\|)\, (p(\mathbf{x}') - p(\mathbf{x}))\, \frac{\xi_i}{\|\boldsymbol{\xi}\|^2} \mathrm{d}V_\xi + g_i, \end{aligned} \tag{1}$$

and the nonlocal divergence-free condition

$$\int_{\mathcal{H}} \gamma\, \omega(\|\boldsymbol{\xi}\|)\, (u_i(\mathbf{x}') - u_i(\mathbf{x}))\, \frac{\xi_i}{\|\boldsymbol{\xi}\|^2} \mathrm{d}V_\xi = 0, \tag{2}$$

where $\mathbf{x}$ is a Eulerian material particle and $\mathbf{x}'$ is a neighboring particle separated by a finite distance. $\mathcal{H}$ is the set of all $\mathbf{x}'$ within a support region parametrized by ϵ. We also employ the shorthand $\boldsymbol{\xi} = \mathbf{x}' - \mathbf{x}$. The u_i are velocity vector components, g_i the external acceleration sources, and p is the fluid pressure. $\underline{\nu}$ is a two-point (between $\mathbf{x}'$ and $\mathbf{x}$) dynamic viscosity. ρ_o is the density. Below we'll show that this nonlocal form converges to the the classical local version for arbitrary $\omega(\|\boldsymbol{\xi}\|)$, and also show what the scaling functions γ and β should be for a given $\omega(\|\boldsymbol{\xi}\|)$. For completeness, the classical Navier–Stokes equations for incompressible flow are

$$\frac{\partial \mathbf{u}}{\partial t} + \mathbf{u} \cdot \nabla \mathbf{u} - \nu \nabla^2 \mathbf{u} = -\frac{1}{\rho_o} \nabla p + \mathbf{g}, \tag{3}$$

with the divergence free condition

$$\nabla \cdot \mathbf{u} = 0.$$

In the interest of brevity we'll show only the convergence of the convective and Laplacian terms from (1) to their local analogues in (3). For the convective term we'll start by Taylor expanding the velocity vector $\mathbf{u}$ about $\mathbf{x}' = \mathbf{x}$, i.e.

$$u_i(\mathbf{x} + \boldsymbol{\xi}) = u_i(\mathbf{x}) + \frac{\partial u_i}{\partial x_k}\xi_k + O(\|\boldsymbol{\xi}\|^2).$$

Substituting the Taylor expansion into the second term of (1) and simplifying, we have

$$\begin{aligned}
u_j(\mathbf{x}) \int_{\mathcal{H}} \gamma\, \omega(\|\boldsymbol{\xi}\|)\, (u_i(\mathbf{x}') - u_i(\mathbf{x}))\, \frac{\xi_j}{\|\boldsymbol{\xi}\|^2} \mathrm{d}V_\xi & \\
&= u_j(\mathbf{x})\, \gamma \int_{\mathcal{H}} \frac{\omega(\|\boldsymbol{\xi}\|)}{\|\boldsymbol{\xi}\|^2} \left(u_i(\mathbf{x})\xi_j + \frac{\partial u_i}{\partial x_k}\xi_k\xi_j - u_i(\mathbf{x})\xi_j \right) \mathrm{d}V_\xi + O(\|\epsilon\|), \\
&= u_j(\mathbf{x}) \frac{\partial u_i}{\partial x_k} \gamma \int_{\mathcal{H}} \omega(\|\boldsymbol{\xi}\|) \frac{\xi_k\xi_j}{\|\boldsymbol{\xi}\|^2} \mathrm{d}V_\xi + O(\|\epsilon\|), \\
&= u_j(\mathbf{x}) \frac{\partial u_i}{\partial x_k} \delta_{kj} + O(\epsilon), \\
&= u_j(\mathbf{x}) \frac{\partial u_i}{\partial x_j} + \cancelto{0 \text{ as } \epsilon \to 0}{O(\epsilon)}, \\
&= \mathbf{u} \cdot \nabla \mathbf{u},
\end{aligned}$$

where δ_{kj} is the Kronecker-delta function, i.e.

$$\delta_{kj} = \begin{cases} 1 & \text{for } k = j, \\ 0 & \text{otherwise.} \end{cases}$$

Demonstrating that the nonlocal convective term converges to the local convection term in the limit as $\epsilon \to 0$, with $\gamma = \frac{3}{m_1}$ assuming that ω is a spherical function, i.e. $\omega(\|\boldsymbol{\xi}\|) = \omega_s(\|\boldsymbol{\xi}\|)$. m_1 is given by

$$m_1 = \int_{\mathcal{H}} \omega_s(\|\boldsymbol{\xi}\|) \frac{\xi_i\xi_i}{\|\boldsymbol{\xi}\|^2} \mathrm{d}V_\xi.$$

In the above we have exploited the symmetry of the integrand in the term $\int_{\mathcal{H}} \omega_s(\|\boldsymbol{\xi}\|) \frac{\xi_k\xi_j}{\|\boldsymbol{\xi}\|^2} \mathrm{d}V_\xi$ to notice that the integrand will be zero except with $i = j$, therefore we can evaluate the integral in polar coordinates as

$$\begin{aligned}
\int_{\mathcal{H}} \omega_s(\|\boldsymbol{\xi}\|) \frac{\xi_k\xi_j}{\|\boldsymbol{\xi}\|^2} \mathrm{d}V_\xi &= \delta_{kj} \int_{\mathcal{H}} \omega_s(\|\boldsymbol{\xi}\|) \frac{\xi_1^2}{\|\boldsymbol{\xi}\|^2} \mathrm{d}V_\xi, \\
&= \delta_{kj} \int_0^{2\pi} \int_0^{\pi} \int_0^{\epsilon} \omega_s(r) \frac{\xi_1^2}{r^2} r^2 \sin(\theta) \mathrm{d}r \mathrm{d}\theta \mathrm{d}\phi, \\
&= \delta_{kj} \frac{m_1}{3},
\end{aligned}$$

where $\xi_1 = r\sin(\theta)\cos(\phi)$, $\xi_2 = r\sin(\theta)\sin(\phi)$, and $\xi_3 = r\cos(\theta)$.

Now we'll employ the same approach for the Laplacian term. Using the following Taylor expansions about $\mathbf{x}' = \mathbf{x}$

$$u_i(\mathbf{x}+\boldsymbol{\xi}) = u_i(\mathbf{x}) + \frac{\partial u_i}{\partial x_j}\xi_j + \frac{1}{2}\frac{\partial^2 u_i}{\partial x_j \partial x_k}\xi_j\xi_k + O(\|\boldsymbol{\xi}\|^3),$$

$$\underline{\nu}(\mathbf{x},\boldsymbol{\xi}) = \underline{\nu}(\mathbf{x},\mathbf{0}) + \frac{\partial \underline{\nu}(\mathbf{x},\mathbf{0})}{\partial \xi_n}\xi_n + O(\|\boldsymbol{\xi}\|^2),$$

$$\underline{\nu}(\mathbf{x}+\boldsymbol{\xi},-\boldsymbol{\xi}) = \underline{\nu}(\mathbf{x},\mathbf{0}) + \frac{\partial \underline{\nu}(\mathbf{x},\mathbf{0})}{\partial x_n}\xi_n - \frac{\partial \underline{\nu}(\mathbf{x},\mathbf{0})}{\partial \xi_n}\xi_n + O(\|\boldsymbol{\xi}\|^2),$$

and substituting into the third term of (1) and simplifying, we have

$$\begin{aligned}
&\int_{\mathcal{H}} \beta\,\omega(\|\boldsymbol{\xi}\|)\frac{\xi_i\left(\underline{\nu}(\mathbf{x},\mathbf{x}') + \underline{\nu}(\mathbf{x}',\mathbf{x})\right)\xi_j}{\|\boldsymbol{\xi}\|^2}(u_j(\mathbf{x}') - u_j(\mathbf{x}))\mathrm{d}V_{\boldsymbol{\xi}} \\
&\qquad = \int_{\mathcal{H}} \beta\,\omega(\|\boldsymbol{\xi}\|)\frac{\xi_i\left(2\underline{\nu}(\mathbf{x},\mathbf{0}) + \frac{\partial \underline{\nu}(\mathbf{x},\mathbf{0})}{\partial x_n}\xi_n + O(\|\boldsymbol{\xi}\|^2)\right)\xi_j}{\|\boldsymbol{\xi}\|^2} \\
&\qquad\quad \times\left(\frac{\partial u_j}{\partial x_m}\xi_m + \frac{1}{2}\frac{\partial^2 u_j}{\partial x_m \partial x_n}\xi_m\xi_n + O(\|\boldsymbol{\xi}\|^3)\right)\mathrm{d}V_{\boldsymbol{\xi}}.
\end{aligned}$$

Collecting terms while recognizing that any odd power of the ξ_i's will integrate to zero due to symmetry of the integrand we have

$$\begin{aligned}
&= \beta\int_{\mathcal{H}} \frac{\omega(\|\boldsymbol{\xi}\|)}{\|\boldsymbol{\xi}\|^2}\left(\xi_n\xi_i\underline{\nu}\xi_j\xi_m\frac{\partial^2 u_j}{\partial x_m\partial x_n} + \frac{\partial u_j}{\partial x_m}\xi_n\xi_i\frac{\partial \underline{\nu}}{\partial x_n}\xi_j\xi_m\right)\mathrm{d}V_{\boldsymbol{\xi}} + O(\epsilon^2), \\
&= (\delta_{ij}\delta_{nm}\nu)\frac{\partial}{\partial x_n}\left(\frac{\partial u_j}{\partial x_m}\right) + \left(\frac{\partial u_j}{\partial x_m}\right)\frac{\partial(\delta_{ij}\delta_{nm}\nu)}{\partial x_n} + O(\epsilon^2), \\
&= \frac{\partial}{\partial x_n}\left((\delta_{ij}\delta_{nm}\nu)\frac{\partial u_j}{\partial x_m}\right) + \cancelto{0 \text{ as } \epsilon\to 0}{O(\epsilon^2)}, \\
&= \nu\frac{\partial^2 u_i}{\partial x_n \partial x_n}, \\
&= \nu\nabla^2\mathbf{u},
\end{aligned}$$

where

$$\delta_{ij}\delta_{nm}\nu = \beta\underline{\nu}\int_{\mathcal{H}} \omega(\|\boldsymbol{\xi}\|)\frac{\xi_n\xi_i\xi_j\xi_m}{\|\boldsymbol{\xi}\|^2}\mathrm{d}V_{\xi},$$

demonstrating convergence of the nonlocal Laplacian term to the classic local one. In the above we have again exploited the symmetry of the integrand in the term $\int_{\mathcal{H}} \omega(\|\boldsymbol{\xi}\|)\frac{\xi_n\xi_i\xi_j\xi_m}{\|\boldsymbol{\xi}\|}\mathrm{d}V_{\xi}$ to notice

that the integrand will be zero for any odd combination of the indices, therefore we can evaluate the integral in polar coordinates as

$$\begin{aligned}\int_{\mathcal{H}} \omega_s(\|\boldsymbol{\xi}\|)\frac{\xi_n\xi_i\xi_j\xi_m}{\|\boldsymbol{\xi}\|^2}\mathrm{d}V_\xi &= \Big(\delta_{ni}\delta_{jm}(1-\delta_{nm}) + \delta_{nj}\delta_{im}(1-\delta_{ij}) + \delta_{nm}\delta_{ij}(1-\delta_{nj})\Big)\int_{\mathcal{H}}\frac{\xi_1^2\xi_2^2}{\|\boldsymbol{\xi}\|^2}\mathrm{d}V_\xi \\ &\quad + \delta_{nm}\delta_{ij}\delta_{nj}\int_{\mathcal{H}}\frac{\xi_1^4}{\|\boldsymbol{\xi}\|^2}\mathrm{d}V_\xi, \\ &= \Big(\delta_{ni}\delta_{jm}(1-\delta_{nm}) + \delta_{nj}\delta_{im}(1-\delta_{ij}) + \delta_{nm}\delta_{ij}(1-\delta_{nj})\Big)\frac{m_2}{15}, \\ &\quad + 3\delta_{nm}\delta_{ij}\delta_{nj}\frac{m_2}{15}, \\ &= (\delta_{ni}\delta_{jm} + \delta_{nj}\delta_{im} + \delta_{nm}\delta_{ij})\frac{m_2}{15}.\end{aligned}$$

Now we equate the result with the substitution we made involving the two-point and classical dynamic viscosity,

$$\begin{aligned}\delta_{nm}\delta_{ij}\nu &= \underline{\nu}\,\beta(\delta_{ni}\delta_{jm} + \delta_{nj}\delta_{im} + \delta_{nm}\delta_{ij})\frac{m_2}{15} \\ 3\delta_{ij}\nu &= \underline{\nu}\,\beta\,\delta_{ij}\frac{m_2}{3} \\ \nu &= \underline{\nu}\,\beta\,\frac{m_2}{9}\end{aligned}$$

So that we notice the nonlocal two-point dynamic viscosity is equivalent to the local viscosity $\underline{\nu} = \nu$ if $\beta = \frac{9}{m_2}$ and

$$m_2 = \int_{\mathcal{H}} \omega_s(\|\boldsymbol{\xi}\|)\xi_i\xi_i\mathrm{d}V_{\boldsymbol{\xi}}$$

In the demonstration above, *no restrictions* where placed on $\omega(\|\boldsymbol{\xi}\|)$, a function that modifies the kernel, giving us complete generality to choose this function based on course-graining information from scales unresolved to those modeled or from experimental and/or phenomenological observation. However, if we do chose $\omega(\|\boldsymbol{\xi}\|)$ in the following form

$$\omega_{ij}(\|\boldsymbol{\xi}\|) = -\frac{C_{n,s}}{2\beta\xi_i\xi_j\|\boldsymbol{\xi}\|^{n+2s-2}}$$

with a normalizing constant $C_{n,s}$ for dimension n and fractional-order s, and $\underline{\nu} = \nu$, we have the special case of the fractional Laplacian if $\varepsilon \to \infty$, i.e. $\mathcal{H} = \mathbb{R}^n$. The other terms in (1) can be shown to be generalizations of both the classic local theory and the fractional derivative models following similar logic as above.

Fractional elasticity as a special case of peridynamics

It's somewhat redundant, but in the subsequent chapters we will borrow notation and ideas from peridynamic mechanics to model nonlocal fluid and mass trasnport. Therefore it is useful

to briefly demonstrate peridynamics as a generalization of fractional derivative based mechanics models, consider the fractional elasticity model of [7]. In this work the authors propose a nonlocal elasticity model, in the spirit of [14], where the stress $\sigma(x)$ takes on a special weighted integral of the strain $\varepsilon(x)$ field

$$\sigma(x) = \frac{E^*}{2\Gamma(1-\alpha)} \int_a^b \frac{\varepsilon(x')}{|x'-x|^\alpha} \mathrm{d}x' = E^* I_{a,b}^{1-\alpha} \varepsilon(x), \tag{4}$$

where $I_{a,b}^{1-\alpha}$ is the fractional Riesz integral operator [1] with fractional order $0 < \alpha < 1$, Γ is the Gamma function, and E^* is the fractional stiffness with anomalous units of $[F][L]^{\alpha-3}$. Utilizing the definition of fractional derivatives, i.e.

$$D^\alpha f(x) = D^n [I^{n-\alpha} f(x)],$$

where D^α is the fractional derivative operator[1] of order α, we can write the equilibrium equation compactly as

$$0 = D_{a,b}^\alpha \left[E^* \varepsilon(x) \right] + b(x),$$

with $b(x)$ representing a body force density. Utilizing the integral form of (4) with the definition of strain for displacement u, i.e. $\varepsilon(x) = u_{,x}$, and rewriting slightly we have

$$\begin{aligned} \sigma(x) =& E^* \int_a^b g_\alpha(x'-x) \frac{\partial u}{\partial x'} \mathrm{d}x', \\ =& E^* \int_a^b \frac{\partial}{\partial \xi} (g_\alpha(\xi)) \left[u(x') - u(x) \right] \mathrm{d}x', \end{aligned} \tag{5}$$

where integration-by-parts has been used in the second of (5) and

$$g_\alpha(\xi) = \frac{|\xi|^{-\alpha}}{2\Gamma(1-\alpha)}, \qquad \xi = x' - x.$$

Substituting (5) into the equilibrium equation and evaluating derivatives gives

$$0 = \frac{E^* \alpha(1-\alpha)}{2\Gamma(1-\alpha)} \int_a^b \frac{u(x') - u(x)}{|x'-x|^{\alpha+2}} \mathrm{d}x' + b(x). \tag{6}$$

Comparing this to the one-dimensional peridynamic equilibrium equation utilizing the constitutive equation of [26] and a "horizon" distance equal to the extent of the domain, i.e. $b - a$

$$0 = \int_a^b k(\xi) \frac{u(x') - u(x)}{|x'-x|} \mathrm{d}x' + b(x), \tag{7}$$

we can see that the fractional elasticity theory proposed in [7] is only a special case of the more general peridynamic theory with the restriction that

$$k(\xi) = k_\alpha(\xi) = \frac{\alpha(1-\alpha)}{2E^*\Gamma(1-\alpha)|\xi|^{\alpha+1}}.$$

[1]The fractional derivative operator reduces to the standard derivative operator for integer powers of α.

The physical motivations for a macroscale spatially nonlocal model assume that there is some underlying (i.e. unresolved at the scale modeled) spatial heterogeneity that causes the nonlocal effects. The kernel function in peridynamics is *part of the constitutive model*, i.e. it should be proposed based on physical or phenomenological assumptions and/or observations of the underlying microstructure, not for mathematical convenience (as is the case with fractional derivatives). Therefore in what follows, we dispense with the notion (and restrictions of) fractional derivatives and simply utilize the more general nonlocal operators.

On nonlocal advection-diffusion and its application to viscous fingering

Introduction

The introduction of Brownian motion in 1827 by the famous Scotish botanist Robert Brown and its re-introduction in Albert Einstein's famous paper in 1905 [13] were the first major leaps towards understanding of the diffusion processes. Einstein's work is based on a random walk thought experiment. In this view, particle motion lacks long term memory and follows a Markovian process. Another assumption made by Einstein was that each step taken by the random walker would be a independent step. However, scientific discoveries and statistical observations such Pareto-Levy distribution were finding processes in which a random walker will take uncorrelated but nonuniform steps over fixed intervals [19]. The experimental evidence of such diffusion processes are seen frequently when looking at the diffusion of protein molecules through plasma membrane [2, 31]. Such processes are known as subdiffussion and lead to a mean square displacement that grows slower than a linear relationship with time. On the other end of the spectrum many observations from nature pointed to situations where the random walker might highly correlated steps and possibly nonuniform steps at each time interval. These processes are known as superdiffusion and are typically found to be the preferred searching mechanism used by foraging animals [29]. Subdiffusion and superdiffusion are the two forms of so-called *anomalous diffusion*.

By 1970s researchers were starting to look at the anomalous diffusion cases with more mathematical rigor. Fluid flow in porous media is one of the important engineering examples where anomalous diffusion has been observed. Heterogeneities of sandstone occur over a wide range of length scales. Some of these heterogeneities are so large that no laboratory experiment can possibly take them into account. To add to the problem many of the interesting events inside sandstone are happening at much smaller length scales compared to the large channels present at scales of aquifers or petroleum reservoirs. This means that no control volume can be chosen such that the local theories would generate satisfying results for all length scales. A non-local model has the advantage that its based on the assumption that each point in the media can interact with any other material point sitting within some finite distance, a horizon. This means that if needed any single point in the media has the freedom to be linked through different channels to any other point. This fact removes the problem of selecting the relevant control volumes.

For the problems where non-local interactions play important rules, one cannot use classical

laws such as Fick's law for transport. We now have the need to introduce new governing equations that are based on functions that are evaluated at two points instead of a single point. These functions are called two-point or long range functions. Silling [27] introduced peridynamics approach to model elasticity and material failure in solid mechanics. The work of Bobaru and Duangpanya [4,5] extended Silling's work to isotropic transient heat diffusion. The work was further extended to advection-diffusion problems in the works of Gunzburger et al. [10,11]. Katyar et al. [17] moved the focus to anisotropic materials and discussed the case of a transient fluid flow in porous and fractured media. In this chapter we will introduce a non-local advection diffusion model for two-phase flow in porous media. We will specifically explore the fluid interaction as the viscosity ratio between the dispersed and dispersing phase is varied.

Viscous fingering is generally referred to the formation of instabilities in the interface of flows through porous media. Saffman and Taylor [23] were among the first to explore this instability. In their research they discussed that when the more viscous fluid is used to disperse the less viscous fluid the interface remains stable. However if the flow is reversed, the less viscous fluid would form channels through the second phase. The understanding of this idea has significant importance in petroleum engineering [22]. A more recent work by Jha [15] has explored the influence of the formation of fingers on the level of mixing of the two phases.

The non-local models presented in the sequel have the ability regularize the moving interface singularities in the mixing domain and at the same time capture interesting instabilities that arise due to the phase interaction. We will show results of viscous fingering simulations and illustrate the convergence of the nonlocal solutions to the local solutions of both pressure and concentration.

Local Advection-Diffusion formulation

Taking the appropriate assumptions, the advection diffusion equation in non-dimensionalized format would take the following form.

$$\frac{\partial c}{\partial t} + \nabla \cdot \left(\boldsymbol{u} c - \frac{1}{Pe} \nabla c \right) = 0 \tag{8}$$

In this equation $\boldsymbol{u}$ is the velocity, c is the non-dimensionalized concentration and Pe is the Peclet number. The assumptions taken for our two phase flow are as follows:

- First contact miscible
- Neutrally buoyant
- Incompressible
- Constant diffusivity

One can further assume that heterogeneities in the domain are larger than the grain size and therefore state that the medium of interest is isotropic on grain scale. With this assumption we can safely

state and use Darcy's law. This law relates velocity to pressure and viscosity and together with our divergence free condition, makes the simplification of the ADE possible.

$$\boldsymbol{u} = -\frac{1}{\mu(c)}\nabla p \quad , \quad \nabla \cdot \boldsymbol{u} = 0 \tag{9}$$

Above p is pressure, μ is the kinematic viscosity and c is af before, dimenshinless concentration, which takes values of one for the less viscous and zero for the more viscous fluid. It is understood that kinematic viscosity can be predicted based on concentration. In this paper we assume viscosity to be an exponential function of concentration and give it the form:

$$\mu(c) = e^{R(1-c)} \tag{10}$$

Here R is defined as $log(M)$ and $M = \frac{\mu_2}{\mu_1}|_{t=0}$. We also have an expression for the Peclet number.This number gives a sense for the importance of advection term compared to the diffusion term.

$$Pe = \frac{UW}{D} \tag{11}$$

In (11), U is the bulk velocity of the flow, W is the width of our control volume and D is the diffusivity between the two fluid phases.
Having taken the required assumptions and introduced the needed definitions, we can start to expand and simply equation (8).

$$\begin{aligned}
&\frac{\partial c}{\partial t} + \nabla \cdot \left(\boldsymbol{u}c - \frac{1}{Pe}\nabla c\right) = 0, \quad \nabla \cdot \boldsymbol{u} = 0 \\
&\frac{\partial c}{\partial t} + \boldsymbol{u}\nabla c - \frac{1}{Pe}\Delta c = 0 \\
&\frac{\partial c}{\partial t} - \frac{1}{\mu(c)}\nabla p \nabla c - \frac{1}{Pe}\Delta c = 0
\end{aligned} \tag{12}$$

Similar procedure can be carried out on equation set (9).

$$\begin{aligned}
&\nabla \cdot \left(-\frac{1}{\mu(c)}\nabla p\right) = 0 \\
&-\nabla(\frac{1}{\mu(c)})\nabla p - \frac{1}{\mu(c)}\Delta p = 0 \\
&-\nabla(e^{-R(1-c)})\nabla p - \frac{1}{\mu(c)}\Delta p = 0 \\
&-R\frac{1}{\mu(c)}\nabla c \nabla p - \frac{1}{\mu(c)}\Delta p = 0 \\
&R\nabla c \nabla p + \Delta p = 0
\end{aligned} \tag{13}$$

Therefore the pair of equations that fully define our two phase flow are the followings:

$$\begin{aligned}
&\frac{\partial c}{\partial t} - \frac{1}{\mu(c)}\nabla p \nabla c - \frac{1}{Pe}\Delta c = 0 \\
&R\nabla c \nabla p + \Delta p = 0
\end{aligned} \tag{14}$$

In this document we will present a non-local set of equations that will recover the set of local (14) for the limit of horizon size approaching zero. This recovery is proved by presenting convergence studies for pressure and concentration of a 1D case study. These non-local equations replace the differential operator of the ADE by integral terms and therefore require significantly higher computational time.They however have the capabilities of handling discontinuities in the domain of interest. In what follows we present a mathematical representation of our proposed model and investigate its properties more thoroughly.

Mathematical model

Before introducing the model we need to clarify the idea of "horizon" of a point which we have already informally introduce and will frequently use. Non-local equations have an advantage over the local equations as they allow each point in the domain to interact with particles sitting a finite distance away from it. We call this zone the horizon of the point. This interaction is exactly what happens in the real world and producing a model that can capture this can have several advantages for the scientific community. The way we implement this idea in our model is to form neighborhood tables for each node and in it place details of any other nodes that seat inside the horizon of this node. Figure 1 clarifies this concept by showing the horizon for 3 randomly chosen nodes in the domain. In this domain we have chosen a periodic boundary condition for our top and bottom boundaries thus the nodes on the very top of the domain will see the bottom nodes as their neighbors and vice versa. This is why a node placed at the bottom edge(here shown in blue) has half of its neighbors on the top boundary of the domain.

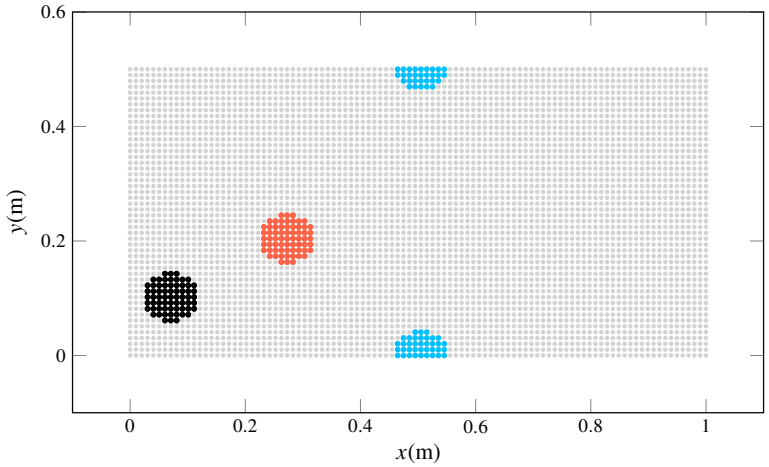

Figure 1: Illustration of how horizon of a point can be split at the edges of the domain

The central idea in this section is to use the Taylor series expansion of pressure and concentration in order to arrive at a set of integral terms which would be identical to our local differential terms

at the limit of horizon size going to zero. Our proposed model is given by (15). In what follows we explore set (14) term by term to arrive at our proposed model.

$$\begin{aligned}
&\frac{\partial c}{\partial t} - \frac{1}{\mu(c)} \int_H \gamma\omega(|\boldsymbol{\xi}|) \left(p(\mathbf{x}+\xi) - p(\mathbf{x})\right) \frac{\xi_i}{|\boldsymbol{\xi}|^2} d\boldsymbol{\xi} \int_H \gamma\omega(|\boldsymbol{\xi}|)(c(\mathbf{x}+\xi) - c(\mathbf{x})) \frac{\xi_i}{|\boldsymbol{\xi}|^2} d\boldsymbol{\xi} \\
&- \frac{2}{Pe} \int_H \gamma \frac{\omega(|\boldsymbol{\xi}|)}{|\boldsymbol{\xi}|^2} (c(\mathbf{x}+\boldsymbol{\xi}) - c(\mathbf{x})) d\boldsymbol{\xi} = 0 \\
&R \int_H \gamma\omega(|\boldsymbol{\xi}|) \left(p(\mathbf{x}+\xi) - p(\mathbf{x})\right) \frac{\xi_i}{|\boldsymbol{\xi}|^2} d\boldsymbol{\xi} \int_H \gamma\omega(|\boldsymbol{\xi}|)(c(\mathbf{x}+\xi) - c(\mathbf{x})) \frac{\xi_i}{|\boldsymbol{\xi}|^2} d\boldsymbol{\xi} \\
&+ \int_H 2\gamma \frac{\omega(|\boldsymbol{\xi}|)}{|\boldsymbol{\xi}|^2} (p(\mathbf{x}+\boldsymbol{\xi}) - p(\mathbf{x})) d\boldsymbol{\xi} = 0
\end{aligned} \tag{15}$$

Gradient In this section we make use of Taylor series expansions of our variables together with our basic knowledge of the results that we are trying to get. Qiang Du et al. [10, 11] rigorously prove what group of non-local equations would converge to the local gradient and divergence terms for horizon size of infinitely small. Their work is motivated by the desire to find a theory similar to the divergence theory but for the case of two point functions. Their proofs are very lengthy and outside the scope of this paper. In this paper we start the forms suggested by [11] and present a mathematical proof of their convergence for the limit case for the convergence terms. We have a similar thought process to arrive at the admissible form for the Laplacian terms which we will discuss further in the next section. Let us now put our focus on the gradient terms. Taylor expansion of pressure about $\boldsymbol{\xi} = \mathbf{0}$ is given by (16). This result can be used to express gradient of pressure as an integral.

$$p(\mathbf{x}+\boldsymbol{\xi}) = p(\mathbf{x}) + \frac{\partial p}{\partial x_j}(\mathbf{x})\xi_j + O(|\boldsymbol{\xi}|^2) \tag{16}$$

$$\begin{aligned}
\Rightarrow \int_H \gamma\omega(|\boldsymbol{\xi}|) \left(p(\mathbf{x}+\xi) - p(\mathbf{x})\right) \frac{\xi_i}{|\boldsymbol{\xi}|^2} d\boldsymbol{\xi} &= \gamma \int_H \frac{\omega(|\boldsymbol{\xi}|)}{|\boldsymbol{\xi}|^2} (p(\mathbf{x})\xi_i + \frac{\partial p}{\partial x_j}(\mathbf{x})\xi_i\xi_j - p(\mathbf{x})\xi_i) d\boldsymbol{\xi} + O(\epsilon^3) \\
&= \frac{\partial p}{\partial x_j}(\mathbf{x})\gamma \int_H \omega(|\boldsymbol{\xi}|) \frac{\xi_j\xi_i}{|\xi|^2} d\boldsymbol{\xi} + O(\epsilon^3) \\
&= \frac{\partial p}{\partial x_j}(\mathbf{x})\delta_{ji} + O(\epsilon^3) \\
&= \frac{\partial p}{\partial x_i}(\mathbf{x}) + O(\epsilon^3)
\end{aligned} \tag{17}$$

Here $\omega = \omega(\mathbf{x} + \xi) = \omega(|\xi|)$ is assumed to be spherically symmetric which implies that:

$$\begin{aligned}\int_H \omega_s(|\boldsymbol{\xi}|)\frac{\xi_k\xi_j}{|\boldsymbol{\xi}|^2}dV_\xi =& \delta_{kj}\int_H \omega_s(|\boldsymbol{\xi}|)\frac{\xi_1^2}{|\boldsymbol{\xi}|^2}d\boldsymbol{\xi} \\ =& \delta_{kj}\int_0^{2\pi}\int_0^{\pi}\int_0^{\epsilon}\omega_s(|\boldsymbol{\xi}|)\frac{\xi_1^2}{\boldsymbol{\xi}^2}\boldsymbol{\xi}^2 sin\theta d\boldsymbol{\xi} d\theta d\phi \\ =& \delta_{kj}\frac{m_1}{3}\end{aligned} \tag{18}$$

Here:

$$m_1 = \int_H \frac{\omega(|\boldsymbol{\xi}|)}{|\boldsymbol{\xi}|^2}\xi_i\xi_i d\boldsymbol{\xi} \tag{19}$$

and we have used the spherical coordinates, $\xi_1 = |\boldsymbol{\xi}|sin\theta cos\phi, \xi_2 = |\boldsymbol{\xi}|sin\theta sin\phi,$ and $\xi_3 = |\boldsymbol{\xi}|cos\theta$. Above we took:

$$\gamma = \frac{3}{m_1} \tag{20}$$

Identical procedure can be applied to $\nabla c(\mathbf{x})$ term, resulting in the following equation for the case of infinitely small horizon:

$$\int_H \gamma\omega(|\boldsymbol{\xi}|)(c(\mathbf{x}+\xi) - c(\mathbf{x}))\frac{\xi_i}{|\boldsymbol{\xi}|^2}d\boldsymbol{\xi} = \nabla c(\mathbf{x}) + O(\epsilon^3) \tag{21}$$

Laplacian Let us start with the following proposed non-local equation and again use the Taylor expansion approach to show that this integral equation recovers the Laplacian term of the ADE

equation.

$$\begin{aligned}
\frac{2}{Pe}\int_H \gamma\frac{\omega(|\boldsymbol{\xi}|)}{|\boldsymbol{\xi}|^2}(c(\mathbf{x}+\boldsymbol{\xi})-c(\mathbf{x}))d\boldsymbol{\xi} = & \\
&= \frac{2}{Pe}\gamma\int_H \frac{\omega(|\boldsymbol{\xi}|)}{|\boldsymbol{\xi}|^2}(c(\mathbf{x}+\boldsymbol{\xi})-c(\mathbf{x}))d\boldsymbol{\xi} \\
&= \frac{2}{Pe}\gamma\int_H \frac{\omega(|\boldsymbol{\xi}|)}{|\boldsymbol{\xi}|^2}(\frac{\partial c}{\partial x_i}\boldsymbol{\xi}_i + \frac{1}{2}\frac{\partial^2 c}{\partial x_i\partial x_j}\xi_i\xi_j + O(|\boldsymbol{\xi}^3|))d\boldsymbol{\xi} \\
&= \frac{2}{Pe}\gamma\int_H \frac{\omega(|\boldsymbol{\xi}|)}{|\boldsymbol{\xi}|^2}(\frac{1}{2}\frac{\partial^2 c}{\partial x_i\partial x_j}\xi_i\xi_j + O(|\boldsymbol{\xi}^3|))d\boldsymbol{\xi} \\
&= \frac{2}{Pe}\gamma\int_H \frac{\omega(|\boldsymbol{\xi}|)}{|\boldsymbol{\xi}|^2}(\frac{1}{2}\frac{\partial^2 c}{\partial x_i\partial x_j}\xi_i\xi_j)d\boldsymbol{\xi} + O(\epsilon^4) \\
&= \frac{2}{Pe}\gamma\frac{1}{2}\frac{\partial^2 c}{\partial x_i\partial x_j}\int_H \frac{\omega(|\boldsymbol{\xi}|)}{|\boldsymbol{\xi}|^2}(\xi_i\xi_j)d\boldsymbol{\xi} + O(\epsilon^4) \\
&= \frac{1}{Pe}\frac{\partial^2 c}{\partial x_i\partial x_j}\delta_{ij} + O(\epsilon^4) \\
&= \frac{1}{Pe}\frac{\partial^2 c}{\partial x_i\partial x_i} + O(\epsilon^4)
\end{aligned} \tag{22}$$

Here γ and m_1 are the same as before. Similarly we can show that the following equation will converge to the Laplacian of pressure for horizon size going to zero.

$$\int_H 2\gamma\frac{\omega(|\boldsymbol{\xi}|)}{|\boldsymbol{\xi}|^2}(p(\mathbf{x}+\boldsymbol{\xi})-p(\mathbf{x}))d\boldsymbol{\xi} = \Delta p + O(\epsilon^4) \tag{23}$$

Influence function So far we have not discussed the shape of our influence function. There are many choices for this function and while as we have all of the admissible choices should result in a convergence, we still want to find the choice that gives us the highest accuracy for the numerical integration. Here we will discuss the constant and linear cases.

Constant Choosing a constant value such as unity for the influence function means that the same weight is given to all neighbors. This is a very easy case to implement and a good starting point however the convergence rates when using $\omega = 1$ can be very slow. For a one dimensional case, horizon becomes a line with length 2δ and $\gamma = 1/m$.

$$m = 2\times\int_H \boldsymbol{\xi}d\boldsymbol{\xi} = \left[\frac{\boldsymbol{\xi}^2}{2}\right]_0^{+\delta} = \delta^2 \tag{24}$$

Linear Choosing a linear profile for ω can significantly improve the accuracy of the numerical integration. We chose $\omega(\boldsymbol{\xi}) = 1 - \frac{r}{\delta}$, $r = |\boldsymbol{\xi}|$. As before for one dimensional case horizon becomes

a line and we have,

$$m = 2 \times \int_0^{\delta} \left(1 - \frac{\xi}{\delta}\right) \xi d\xi = \left[\frac{\xi^2}{2} - \frac{\xi^3}{3\delta}\right]_0^{\delta} = \frac{\delta^2}{3} \tag{25}$$

For the case of two dimensional domain, horizon takes the form of a circle with radius δ. In this case $\gamma = 2/m$.

$$\begin{aligned} m &= \int_0^{2\pi} \int_0^{\delta} \omega(\xi) \xi d\theta d\xi = \int_0^{2\pi} \int_0^{\delta} \left(1 - \frac{\xi}{\delta}\right) \xi d\theta d\xi = \left[\frac{\xi^2}{2} - \frac{\xi^3}{3\delta}\right]_0^{\delta} \\ &= \frac{\delta^2 \pi}{3} \end{aligned} \tag{26}$$

Results and discussion

In order to verify the proposed moel we have chosen to solve one and two dimensional cases of simple two phase flow problem. In the two dimensional case we have chosen the initial fluid interface to be flat in order to be able to compare results with the results of a finite differencing solution. In both cases the less viscous fluid is pushed into the move viscous one and the excess fluid is allowed to exit from the right boundary of the domain. Section discusses the 2-dimensional case where the initial interface is disturbed to allow the formation of viscous fingers.

Flat Interface In order to validate the derived non-local equations, we chose a classical two dimensional problem with periodic boundary conditions on top and bottom as shown in fig. 1. In this problem the domain is initially saturated with the higher viscousity fluid. The less viscous fluid is then pushed through from the left and the excess fluid is allowed to exit the domain from the right edge of the domain. Our fluids are first contact miscible and so one would expect to see the formation of a mixing region as soon as the two phases meet. Figure 2 shows the setup of this problem.

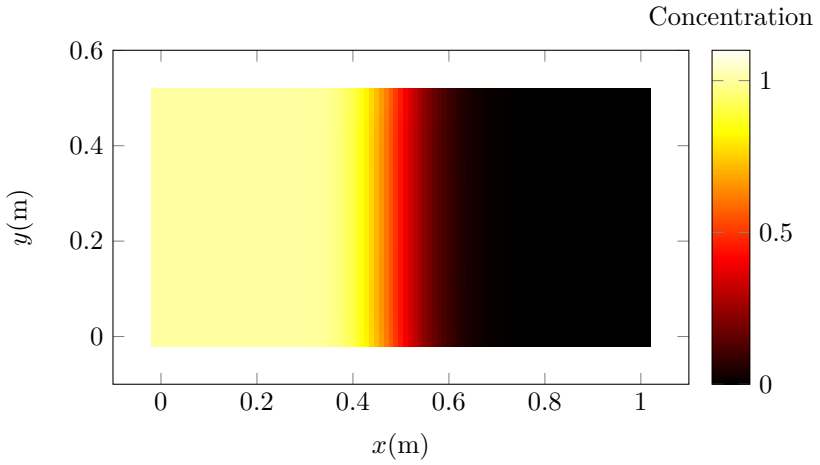

Figure 2: Dispersion of a high viscosity phase with a less viscous flow

There are analytical solutions for a linear problem with the above setup. However, the dependency of viscosity on concentration means that the problem we are interested in is non-linear. Therefore we are required to use a finite differencing scheme in order to verify results of our non-local model.

Finite Differencing Scheme A backward in time, central differencing method was used to calculate solve for the pressure. However, the non-locality in the advection diffusion equation makes this method unstable when solving for concentration. Up-winding was used to stabilize the concentration solution. This method is explicit in both pressure and concentration. The set of equations used are direct translation of equation set (14) with the addition of up-winding to the gradient term of the concentration. It is clear to see that a two dimensional problem with a flat interface between the two phase can be modelled as a one dimensional problem. Therefore to save time and specially for the non-local modeling simulations, the finite difference model was used to solve the equivalent 1D problem. The non-local model was however solved both in one and two dimensions to make sure that the results do in fact match.

Discretization In this problem we have used a uniform grid size throughout the whole of our domain with node spacing $\Delta x = \frac{L}{N}$ where L is the length of the domain and N is the number of nodes on the length. For the 1D case, each node is assigned a length equal to the grid spacing. This number for a 2D case becomes the area of a square with sides equal to Δx. With this at hand we can turn our integral in (15) into finite sums. For every node in the domain,summation is carried out over all the neighboring nodes.

$$
\begin{aligned}
&\frac{c^{n+1}(\mathbf{x}_i) - c^n(\mathbf{x}_i)}{\Delta t} - \frac{1}{\mu(c)} \sum_j \gamma\omega(|\boldsymbol{\xi}|) \left(p^{n+1}(\mathbf{x}_j) - p^{n+1}(\mathbf{x}_i)\right) \frac{\xi_\alpha}{|\boldsymbol{\xi}|^2} A_j \times \sum_j \gamma\omega(|\boldsymbol{\xi}|)(c^{n+1}(\mathbf{x}_j) - c^{n+1}(\mathbf{x}_i)) \frac{\xi_\alpha}{|\boldsymbol{\xi}|^2} A_j \\
&- \frac{2}{Pe} \sum_j \gamma \frac{\omega(|\boldsymbol{\xi}|)}{|\boldsymbol{\xi}|^2} (c^{n+1}(\mathbf{x}_j) - c^{n+1}(\mathbf{x}_i)) A_j = 0 \\
&R \sum_j \gamma\omega(|\boldsymbol{\xi}|) \left(p^{n+1}(\mathbf{x}_j) - p^{n+1}(\mathbf{x}_i)\right) \frac{\xi_\alpha}{|\boldsymbol{\xi}|^2} A_j \times \sum_j \gamma\omega(|\boldsymbol{\xi}|)(c(\mathbf{x}_j) - c(\mathbf{x}_i)) \frac{\xi_\alpha}{|\boldsymbol{\xi}|^2} A_j \\
&+ \sum_j 2\gamma \frac{\omega(|\boldsymbol{\xi}|)}{|\boldsymbol{\xi}|^2} (p^{n+1}(\mathbf{x}_j) - p^{n+1}(\mathbf{x}_i)) A_j = 0
\end{aligned}
\tag{27}
$$

Above A_j can be thought of as Δx^2 for 2-dimensional case and as Δx for the 1D case and α subscript represents x and y directions. Above $\mathbf{x}_j := \mathbf{x}_i + \boldsymbol{\xi}$ where j represent a neighboring node and x_i is the spatial position of the node of interest.

Parametrization We have solved the proposed problem with the following parameters. The domain length, $L = 1$ m, domain height, $h = 0.5$ m, $\mu_1 = 1.0$ and $R = 1.0$. $Pe = 10^4$ and the pressure difference across the right and left edges was set at 1 KPa.

Boundary conditions Imposing the Dirichlet boundary conditions for the non-local model can be done by setting the value of all nodes within a horizon distance from the left and right boundaries equal to the desired value. This ensures that the next node has sees this value coming from all nodes downstream. Imposing the periodic boundary condition can be done by linking the top and bottom nodes together. This can be thought of a rolled paper where now the top and bottom edge nodes are in direct contact. If the neighboring is done in this state, all the nodes within one horizon from the top and bottom would have at least a neighbor on the opposite side. We can now unroll the paper into a flat sheet again and use the generated neighborhoods table to simulate this periodic boundary.

Convergence Study Numerical discretization of our domain means that the exact non-local solution can only be calculated as m approaches infinity while horizon size approaches zero at an even faster rate [11]. All of the results presented here are outcomes of a massively parallel code, but even with the use of a supercomputer to run this code one would not find much sense in increasing m further than a certain point. We ran multiple simulations with a constant horizon size and varying m and found this number to be between 4 and 6. Katiyar et al. [17] have reported very similar values. Having a higher number of nodes inside the horizon will improve the accuracy of the result but at the cost of very high computational time. On the other hand, reducing this density can output unsatisfactory results and in some cases no convergence at all. Running the m-convergence test helps us study the convergence of the model to the exact non-local solution. This exact non-local solution however is not the same as the required local solution. Getting to the local solution is only possible when the discretization is refined at a higher rate as the rate at which m is increased [5, 6]. Here we have decided to ommit the results of the m-convergence test and only present the result of convergence to the local solutions. Following figures show the convergence of our non-local model to solution of the finite differencing scheme of section . Figure 3 shows the convergence of the non-local model to the solution of the one-dimensional advection diffusion problem while similar results for pressure are presented in Figure 22.

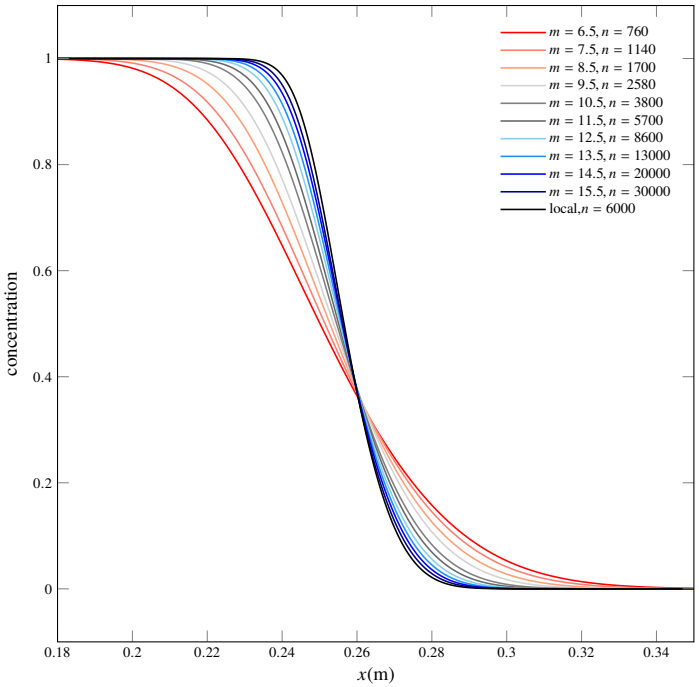

Figure 3: Convergence of concentration

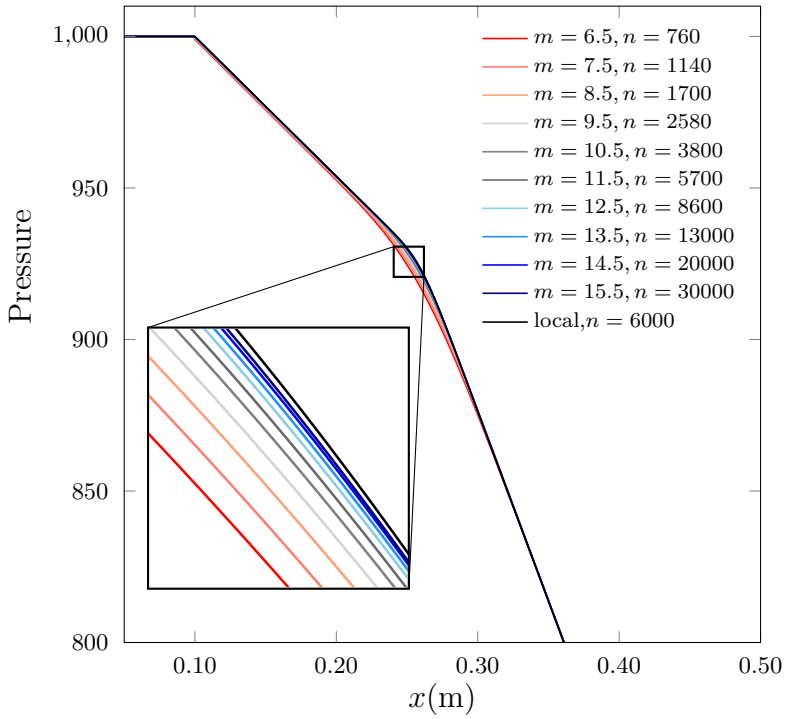

Figure 4: Convergence of pressure

Disturbed Interface Having verified the model against the local solutions for the flat interface problem we can now move to the more complicated case. In their 1958 paper, Saffman and Taylor [23] introduces the idea of Saffman-Taylor instability which is now widely know as viscous fingering. They showed that when a less viscous fluid is used to push a more viscous fluid inside a porous media, the interface becomes instable and channels of the less viscous fluid start to find their way through the viscous phase. Viscous fingering has been since widely studied both by researchers interested in its effects on oil recovery [20] and by those interested in its effect in enhancing fluid mixing [15]. As it happens the advection diffusion equation have built in them all that requires to capture this instability. Therefore we chose this example as our second case study. In this case we would not be able to directly compare numerical results to the literature but we are rather interested in the qualitative features. In what follows we present the results of this study and show that the proposed non-local model is also able to capture this phenomena with it the need for any modification.

Disretization As for the first case we have chosen to use the uniform grid discretization for this simulation. For the specific results presented, $m = 4.5$ and $\Delta x = L/1600$. Peclet number was set at 10000 and $R = 3.0$.

Imposing Boundary Conditions This simulation also has Dirichlet boundaries for left and right edges set as explained in section . The periodic boudary condition for the top and bottom edges were also set as explained before. In this case the formation of the fingures require and initiation. Thus we have decided to initiate a disturbance on the interface at time zero and hold it long enough for the fingers to start formation.

Non-local solution As expected the non-local model was able to capture the viscous fingering phenomena without requiring any adjustment.

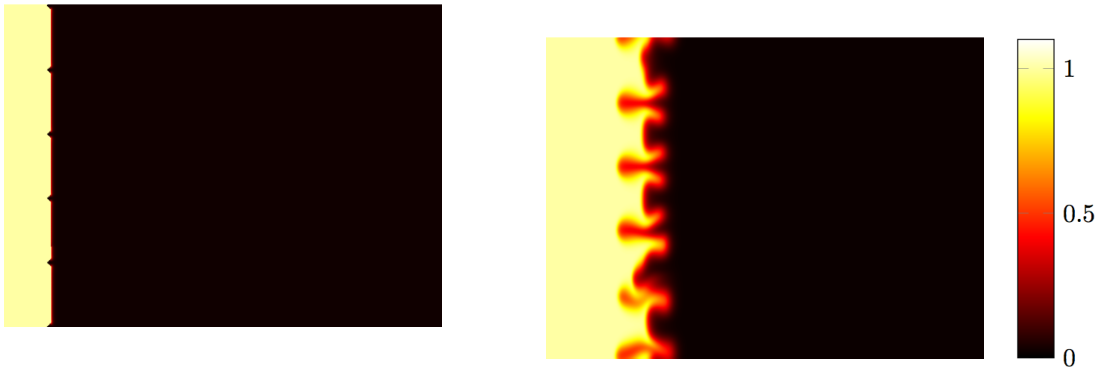

(a) Screen shot taken at time=0 to show the intial disturbed placed at the interface in order to promote the occurance of viscous fingering

(b) After only 3 ms the formation of the fingers have already taken shape. The interactions between adjacent fingers is promoting further disorder

(c) 6.3 ms into the injection and the pressure build up at the finger tips is causing the elongation of the fingers

(d) We are now 8 ms into the injection and we can clearly see the splitting and merging of fingers

Figure 5: Above screen shots follow the evolution of fingers from the injection moment for 8 ms. For this simulation we have chosen the following parameters. $\Delta t = 0.03125$ ms, $\Delta p = 1000$ pa , $R = 3.0, \delta = 3.5$ grid spacings. We are also using a linear weight function.

For a given numerical discretization one would expect so see more dispersion as the horizon size is increased. This is due to the nature of a non-local model and the fact that with a larger horizon the particles are allowed to have direct contact over a more extended area and therefore the interface would seem to get widen as m is increased. To capture this idea mathematically we can introduce a method for computing the mixing degree of our two phase flow. We follow the same definition as [15] provides. The mixing degree X is given by $X(t) = 1 - \sigma^2(t)/\sigma^2_{max}$. Where σ is the varience of the concentration field and σ_{max} is the maximum value is achieves during the

simulation. Figure 6 shows the increase in the degree of mixing as the non-locality is increased.

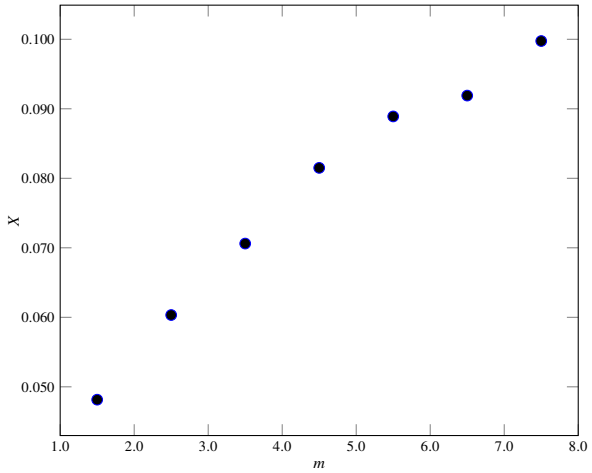

Figure 6: Illustration of the mixing degree based on the calculationg of the varience of concentration field

And now we consider the case when flow direction is reversed and viscous fluid is used to push the less viscous fluid forward.

(a) Snapshot taken at time zero shows the initial disturbance of the boundary between the two phases

(b) 5 ms into the injection and as expected the initial disturbances have become distinct fingers

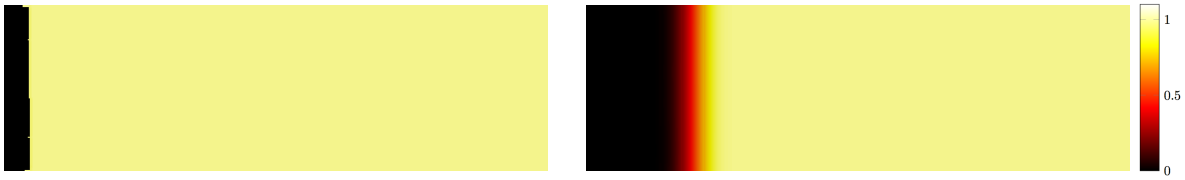

(c) In this case the flow order is reveresed. The more viscous fluid is now used to disperese the less viscous phase.

(d) Above snapshot is taken 1.8 ms after injection. The ease of movement in the less viscous fluid works as a supressant of finger formation

Figure 7: Comparison of the reversed flow case to our original simulation for a viscosity ratio $M = 12.2$, $\Delta p = 1500$ pa and $\Delta t = 0.0125$ ms. The horizon size used for both simulations is 3.5 grid spacing

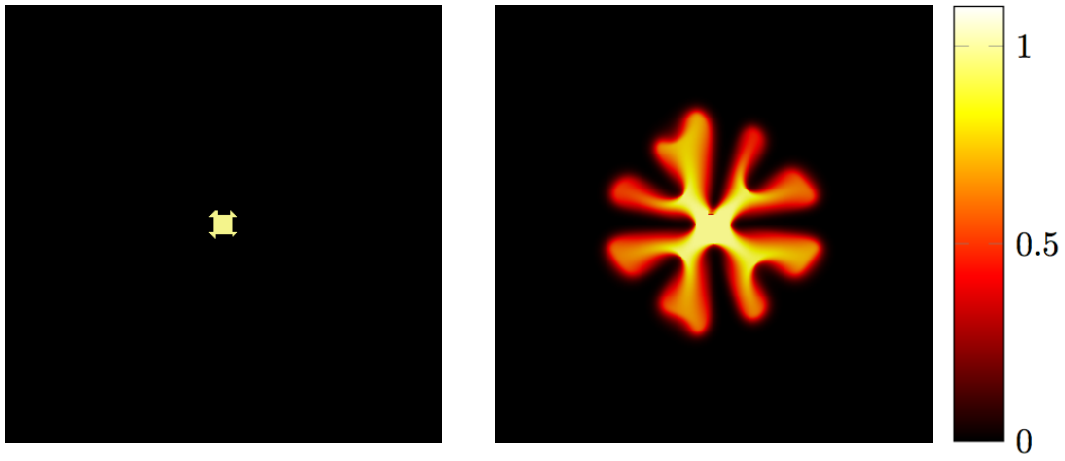

(a) Initial snapshot shows the injection point which is placed at the mid point of our domain.

(b) Formation of viscous fingers is clearly apparent in the snapshots taken at initial stages of injection.

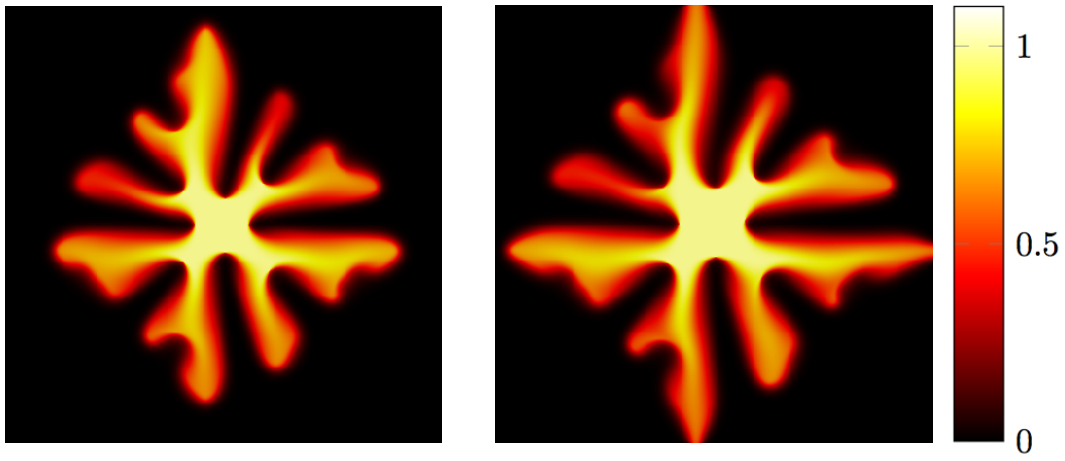

(c) Note the simultaneuos growth of the central inclusion

(d) Symmetry of the domain has stopped tangential interaction of fingers

Figure 8: Central injection was done under pressure difference $\Delta p = 1500$ pa, $R = 3.0$, $\Delta t = 0.00625$ ms. Screen shots are taken on 3 ms intervals.

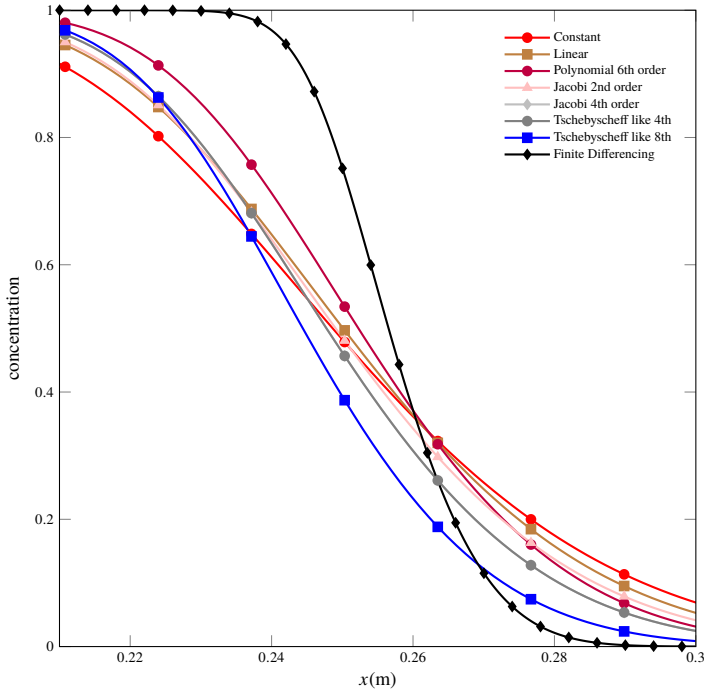

Figure 9: Comparison of results with a wide range of weight functions

Figure 10: Central injection, R=2

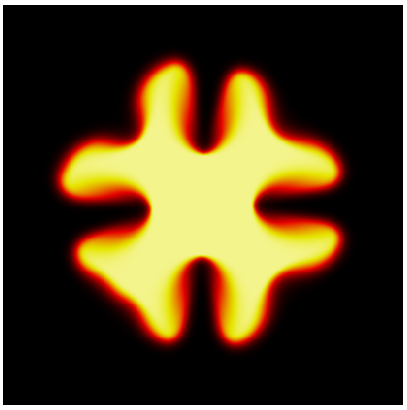

Figure 11: Central injection, R=3

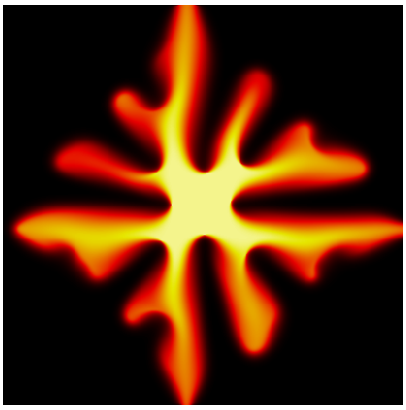

Figure 12: Central injection, R=7

Nonlocal homogenization of nanofluid mixtures

Introduction

Nanofluid is the term used for a suspension made out of nano size metallic or non-metallic particles in a base fluid. Since their introduction, nanofluids have been thought of as one of the most promising advancements in heat transfer properties of fluids [28].

While local equations of fluid dynamics and heat transfer have been successful in modeling fluid behavior in many situations, they have not been so accurate when fluid's structure gets more complex [12, 30]. These equations typically ignore existence of nanoparticles due to their low volumetric ratio and predict no significant improvement in heat conductivity of nanofluids [8]. It seems that to be able to capture true involvement of nanoparticles, an understanding of the molecular structure of the fluid is of the highest importance.

In contradiction to prediction of local equations of heat transfer, experimental work have pointed at significant improvement in the conductivity of nanofluids over their base fluid. However, there is a big discrepancy when it comes to deciding the most effective size or percentage nanoparticle loading. This goes back to the fact that the failure of the current local models result in a lack of theoretical understanding of the processes behind heat transfer in nanofluids.

Molecular dynamic's (MD) models have been much more accurate in their predictions in comparison to local models and thus have become the standard for computational investigations of nanofluids [3,21,24]. These models are capable of accurately capturing the interatomic interactions between base fluid and nanoparticles and therefore have the ability to investigate many different proposed mechanisms. Keblisnksi et al. [18] lists ballistic nature of heat transfer in nanofluids, ordered layering of fluid around nano particles, thermal energy transfer due to Brownian motion of nanoparticles and clustering of highly conductive nanoparticles as the potential mechanisms responsible for the increased heat conductivity. MD models can naturally take all of these points into account.

While MD models are capable modeling tools, almost all molecular dynamic simulations are

run on domains that are far smaller than what is used in real life applications [24]. These models can be an effective tool for understanding of the nature of the nanofluids but lack the ability to capture any macro-scale effects that might be introduced due to the experimental procedure. This is were Non-local models can shine. Non-local models are previously shown to be one of the natural methods in which MD models can be upscaled [25]. This upscaling can both reduce the computational time and increase the ability of the model to capture phenomena occurring at macro-scale. Keeping the accuracy of the results while upscaling however requires some initial work. Non-local models have two important limits. Typically, achieving the local limit of these equations does not require any special treatment. This limit can be used to compare the results against established local models.

There are however certain elements of these models such as the accurate horizon size and shape that can significantly change the non-local limit of the models. This document attempts to explain how each of these elements change the result of non-local convergence and present a method which can be used systematically with any nanofluid to estimate the required horizon size and shape.

Proposed Method for Kernel Extraction

The kernel in a non-local model is widely understood as the representation of the average interaction between material points or particles inside the domain. For the current investigation we are interested in interactions that take part in heat transfer processes. Heat can be understood as the average kinetic energy of individual particles. Forces are the tools for transfer of kinetic energy between particles and as a results they dictate the shape of our nonlocal kernel. The MD model used was setup to use a 6-12 LJ potential for Argon and Copper. The LJ parameters used for Argon and Copper are $\sigma_{\mathrm{Cu}} = 2.3377e-10$, $\epsilon_{\mathrm{Cu}} = 65.625e-21$, $\sigma_{\mathrm{Ar}} = 3.405e-10$ and $\epsilon_{\mathrm{Ar}} = 1.67e-21$. The MD simulation of the same domain was run on both pure Argon and 0.9-7.5% Ar-Cu nanofluid with time step of 1 femtosecond and for 2 million time steps.

The proposed method for kernel extraction includes the position file output from the MD model. The position of individual particles were recorded every 1000 time steps. Choosing particles one by one, the domain was split into spherical shells around the chosen particle. We then sorted the remaining particles into arrays according to their shells and kept this data in a table of neighborhoods. Looping over neighboring particles, we calculated the LJ potential observed from any of the shells. This method allowed us to calculate the average LJ potential on the chosen particle for the 2 million time steps. The process was repreated for every single particle inside the domain and the results of all these LJ potential calculations were also averaged to give us the final plot of LJ potential. The results for pure Argon are plotted on figure 14.

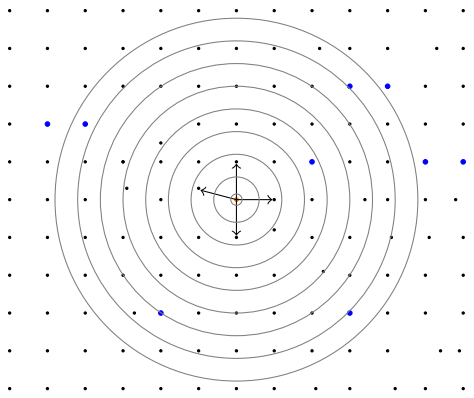

Figure 13: Domain was split into spherical shells to calculate the forces. Here, larger blue dots represent the nanoparticles and small black dots are Argon atoms.

In order to check the convergence of this method, the thickness of the shells were reduced in steps. We were able to show that the potential calculation converges and the result of convergence is close to the analytical LJ potential. Finding the potential in the proposed method has two major advantages over taking the standard LJ graph for Argon.

Firstly, as the slices are made thinner than equilibrium distances between Argon atoms the repulsive forces keep atoms from entering the slices closest to the slice containing the central particle and therefore those slices represent a zero force. This fact will also be mentioned later when we talk about atom distributions shown in figure 17. In the standard LJ potential the force for these closest shells would approach infinity and would have required careful attention. Looking at the atom distribution of fig.17 it is clear that a drop in atom density before and after equilibrium position is expected. These lower atom distribution densities result in a slight deviation of the calculated LJ potential from the expected analytical graph. The second advantage of proposed method is that this method does not lose accuracy as the nanoparticles are introduced into the base fluid. The exact procedure can be followed to find the averaged LJ potential experienced on every particle in any nanofluid.

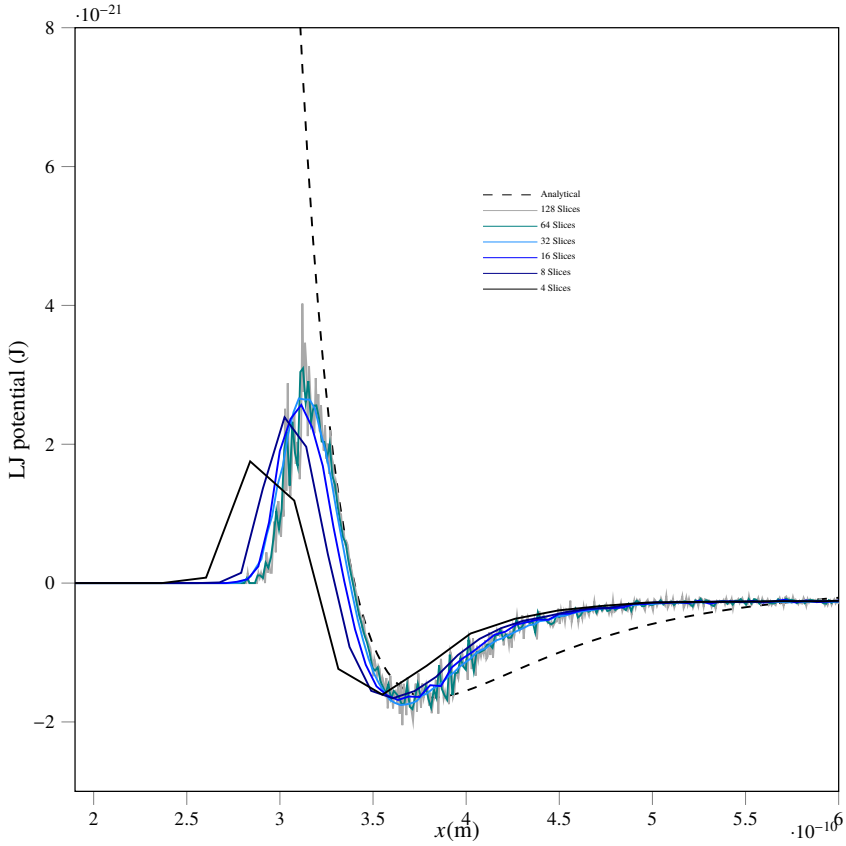

Figure 14: Convergence of the proposed method for LJ potential calculation for pure Argon

Leonard-Jones potentials were calculated for pure liquid argon and Cu-Ar nanofluids with nanoparticle loading between 0.9 and 7.5%. The calculated potentials were then differentiated over distance to give the average radial force experienced from any point in space inside the domain. This force whether negative or positive can help transfer kinetic energy between particles. Therefore the shape of the kernel should be linked to the absolute value of the calculated force. If one assumes that the time average velocity of every particle in the domain is equal, then the proposed method can be closely linked to the infamous Green-Kubo method which has been widely used in previous heat conductivity calculations for nanofluids. The calculated kernels for pure Argon and 3.8% Cu-Ar nanofluid are plotted here.

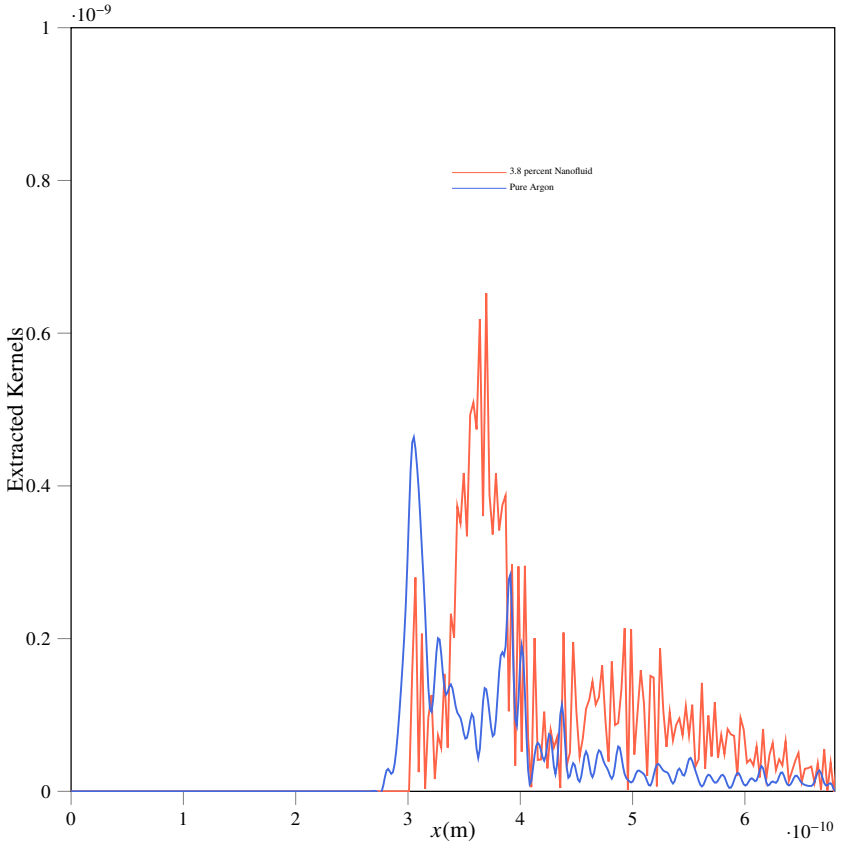

Figure 15: Extracted kernels for pure liquid argon and nanofluid plotted alongside each other

The calculated kernel for pure argon looks very similar to the absolute of the calculated LJ force which is exactly what we would expect. For the nanofluid however, the kernel is far from a simple average of the LJ forces for pure Argon and pure Copper. When exploring the nature of the nanofluid it is clear that some Argon atoms permanently arrange themselves around nanoparticles, essentially adding to the size of nanoparticle. This can be seen in figure 16 which is a screenshot of one of the nanoparticles. What is perhaps more interesting is the particle distributions shown in fig.17. Here, it is shown that these solid like arrangements essentially pack some Argon atoms together closer than normal and as a result force the remaining majority of argon atoms to space themselves out inside the domain. As a consequence, the second peak of the of the fig.17 for 3.8% nanofluid is now placed right after the equilibrium atomic distance for argon instead of being right on top of it. The first peak of this graph represents the highest distribution density for Copper atoms.

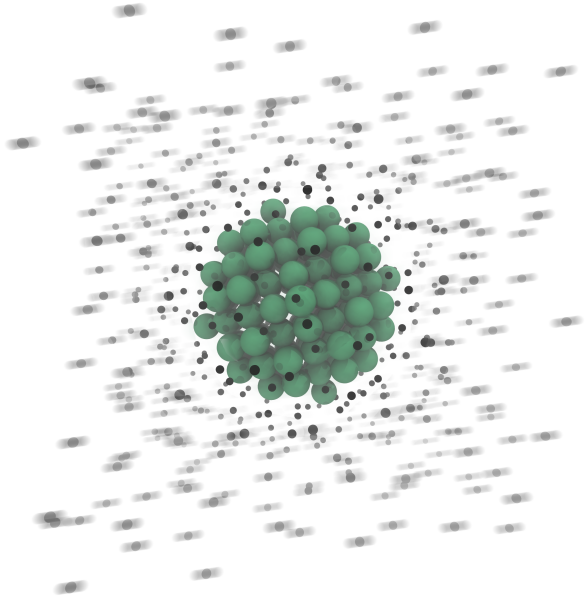

Figure 16: Distribution of Argon atoms around a single Copper nanoparticle. Motion effect is artificially added on a single frame to represent what would be seen on the video

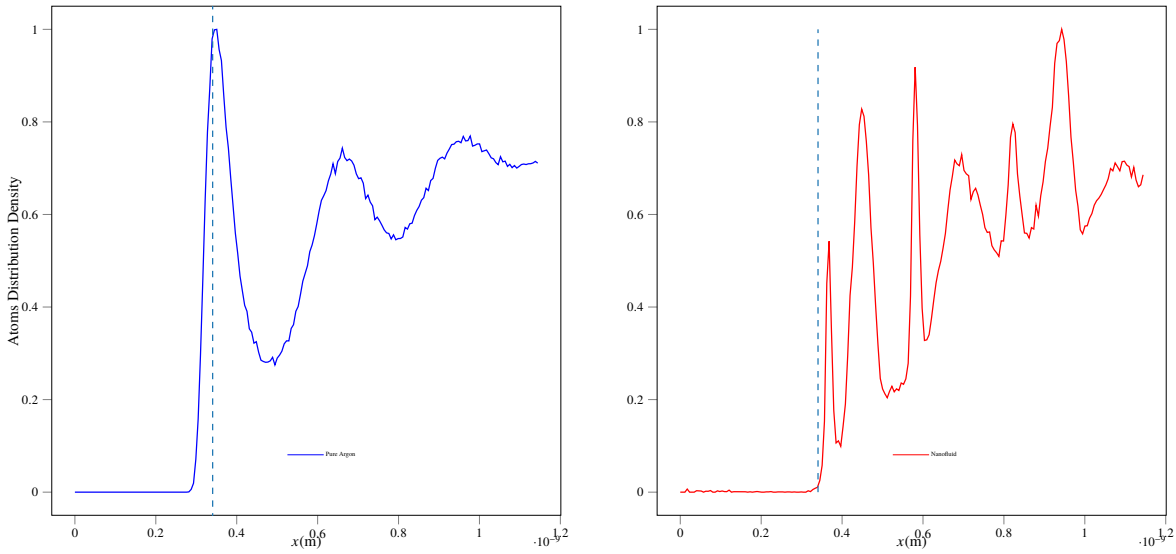

Figure 17: Radial distribution of atoms about a central particle in both pure Argon and nanofluid

As discussed above, the majority of Argon atoms will be forced to space out inside the domain as nanoparticle loading is increased. This should essentially result in a lower heat conductivity

inside the parts of the nanofluid that solely include Argon atoms. On the other hand, as heat reaches the nanoparticle and its surronding solid-like Argon structure, it is very rapidly transfer through the nanoparticle structure. These two processes will always be in oppose to each other and the stronger of the two will dictate the overall change in thermal conductivity of the nanofluid. In order to understand the nature of the calculated nanofluid kernel we decided to plot the LJ potential components of our nanofluid. The three components of the overall LJ potential of the nanofluid are from Ar-Ar, Cu-Cu and Ar-Cu interactions. Figure 18 shows these components. Eventhough the volumetric ratio of Copper is much lower than argon, their very compact structures mean that the number of atoms ratio between Copper and Argon is closer to 15% for the 3.8% volumetric nanofluid. This and the much higher force for Cu-Cu interactions make the graph of the Cu-Cu summed force much more significant compared to the Argon-Argon graph. As discussed this force would result in a rapid transfer of energy and therefore heat through the nanoparticle. Here we will be making an important assumption and that is the limiting elements of our domain in terms of heat transfer are Argon atoms. As long as the heat can effectively pass through the base liquid and reach a nanoparticle, it would almost instantaneously pass through the nanoparticle. and so when considering important forces we will completely ignore the high forces between Copper atoms. Following the same logic we decided to give only 50% importance to Ar-Cu forces and 100% importance to Ar-Ar forces. Doing the weighted average in the above manner resulted the presented kernel on fig.15 for the 3.8% nanofluid.

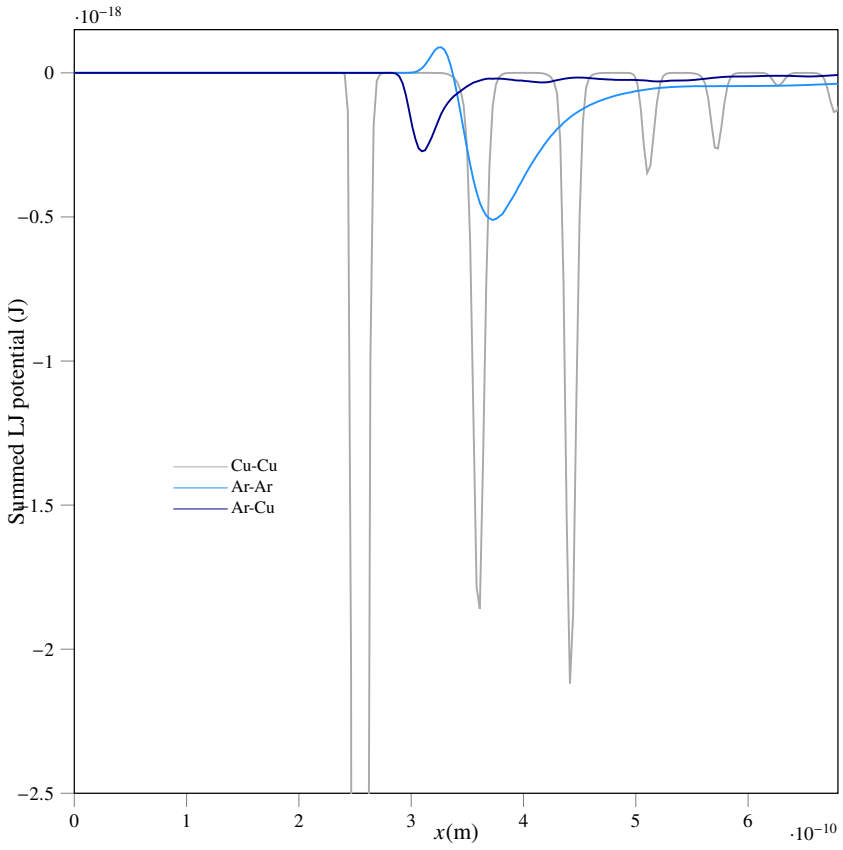

Figure 18: Components of LJ potential from interations between Cu and Ar particles

In order to check the validity of our method we decided to carry out the same calculation for pure Argon and for different nanofluids with volumetric nanoparticle loading between 0.9 and 7.5%. We can integrated the kernel graph for each case. The area under kernel graph in our non-loal model should represent the thermal conductivity of our fluids. The final step of the process is to calibrate the data to link the calculated areas to the correct thermal conductivities. The calibration was done buy setting the area of pure argon equal to 0.127 Wm-1K-1 and the area of 1.8% nanoparticle equal to 0.163 Wm-1K-1. All other points were automatically calculated based on their area ratio to the area of 1.8% nanofluid. The predictions of this model show a close ralationship to the MD predictions based on Green-Kubo method as reported by Sarkar et. al [24]. The Green line shows the prediction of Hamilton-Crosser equation which significantly underpredicts all nanofluid thermal conductivities compared to both MD and our proposed nonlocal model.

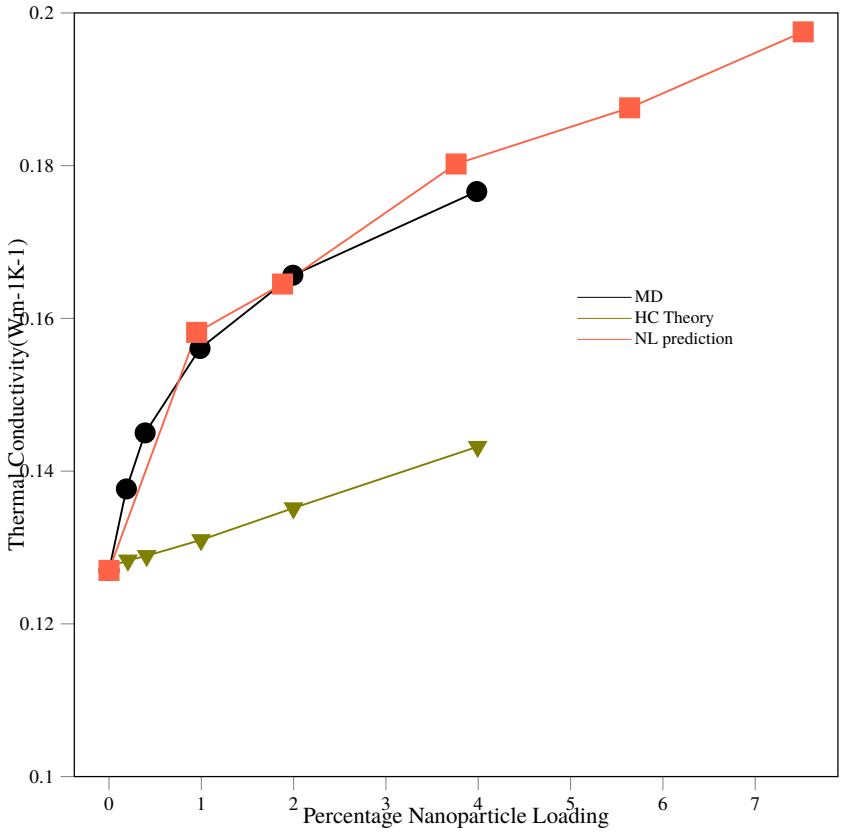

Figure 19: Components of LJ potential from interations between Cu and Ar particles

Going back to the four seggested mechanisms of heat transfer in nanofluids taken by Kebliski et al. [18], our proposed model suggests that the ordering of base fluid around nanoparticles has the highest effect on the heat conductivity of the nanofluids. This fact is in agreement with many previous works who focused on the effect of base fluid layering [16, 32]. Future work focusing on the same method can use a geometrical method to calculate the effective volume of nanoparticles after liquid layering to estimate the ideal radius of nanoparticles.

Non-local Diffusion Model

MD models are usually run on small domains with periodic boundary conditions. It is easy to show that simple central heating problems in these domains do not generate significant convective flows and as a result it is reasonable to assume that the particle velocities in our model are insignificant for our current calculation. Taking this assumption leaves us with the diffusive part of the heat transfer process.

$$0 = \rho c \frac{\partial T}{\partial t} - 2k \int_{\mathcal{H}} \gamma \omega(|\boldsymbol{\xi}|)(T(\mathbf{x}+\boldsymbol{\xi}) - T(\mathbf{x})) \frac{1}{|\boldsymbol{\xi}|^2} \mathrm{d}\boldsymbol{\xi} \tag{28}$$

We can now use Taylor expansion of temperature to prove that the proposed non-local diffusion model will converge to the local diffusion equation.

$$\begin{aligned}
\lim_{\epsilon\to 0}\ 2k\int_{\mathcal{H}}\gamma\frac{\omega(|\boldsymbol{\xi}|)}{|\boldsymbol{\xi}|^2}(T(\mathbf{x}+\boldsymbol{\xi})-T(\mathbf{x}))\mathrm{d}\boldsymbol{\xi} = & \\
&= \lim_{\epsilon\to 0} \quad 2k\gamma\int_{\mathcal{H}}\frac{\omega(|\boldsymbol{\xi}|)}{|\boldsymbol{\xi}|^2}(T(\mathbf{x}+\boldsymbol{\xi})-T(\mathbf{x}))\mathrm{d}\boldsymbol{\xi}, \\
&= \lim_{\epsilon\to 0} \quad 2k\gamma\int_{\mathcal{H}}\frac{\omega(|\boldsymbol{\xi}|)}{|\boldsymbol{\xi}|^2}(\frac{\partial T}{\partial x_i}\xi_i+\frac{1}{2}\frac{\partial^2 T}{\partial x_i\partial x_j}\xi_i\xi_j+O(|\boldsymbol{\xi}^3|))\mathrm{d}\boldsymbol{\xi}, \\
&= \lim_{\epsilon\to 0} \quad 2k\gamma\int_{\mathcal{H}}\frac{\omega(|\boldsymbol{\xi}|)}{|\boldsymbol{\xi}|^2}(\frac{1}{2}\frac{\partial^2 T}{\partial x_i\partial x_j}\xi_i\xi_j+O(|\boldsymbol{\xi}^3|))\mathrm{d}\boldsymbol{\xi}, \\
&= \lim_{\epsilon\to 0} \quad 2k\gamma\int_{\mathcal{H}}\frac{\omega(|\boldsymbol{\xi}|)}{|\boldsymbol{\xi}|^2}(\frac{1}{2}\frac{\partial^2 T}{\partial x_i\partial x_j}\xi_i\xi_j)\mathrm{d}\boldsymbol{\xi}+O(\epsilon^3), \\
&= \lim_{\epsilon\to 0} \quad 2k\gamma\frac{1}{2}\frac{\partial^2 T}{\partial x_i\partial x_j}\int_{\mathcal{H}}\frac{\omega(|\boldsymbol{\xi}|)}{|\boldsymbol{\xi}|^2}(\xi_i\xi_j)\mathrm{d}\boldsymbol{\xi}+O(\epsilon^3), \\
&= \lim_{\epsilon\to 0} \quad k\frac{\partial^2 T}{\partial x_i\partial x_j}\delta_{ij}+O(\epsilon^3), \\
&= \lim_{\epsilon\to 0} \quad k\frac{\partial^2 T}{\partial x_i\partial x_i}+O(\epsilon^3), \\
&= k\nabla^2 T.
\end{aligned}$$

Therefore taking the limit on all terms from equation 28 leaves us with

$$0 = \rho c\frac{\partial T}{\partial t} - k\nabla^2 T \tag{29}$$

Here $\omega = \omega(|\boldsymbol{\xi}|) = \omega_s(|\boldsymbol{\xi}|)$ is assumed to be spherically symmetric which implies that

$$\begin{aligned}
\int_{\mathcal{H}}\omega_s(|\boldsymbol{\xi}|)\frac{\xi_k\xi_j}{|\boldsymbol{\xi}|^2}\mathrm{dV}_\xi =& \delta_{kj}\int_{\mathcal{H}}\omega_s(|\boldsymbol{\xi}|)\frac{\xi_1^2}{|\boldsymbol{\xi}|^2}\mathrm{d}\boldsymbol{\xi}, \\
=& \delta_{kj}\int_0^{2\pi}\int_0^{\pi}\int_0^{\epsilon}\omega_s(|\boldsymbol{\xi}|)\frac{\xi_1^2}{\boldsymbol{\xi}^2}\boldsymbol{\xi}^2 sin\theta\mathrm{d}\xi\mathrm{d}\theta\mathrm{d}\phi, \\
=& \delta_{kj}\frac{m_1}{3}.
\end{aligned}$$

With

$$m_1 = \int_{\mathcal{H}}\frac{\omega(|\boldsymbol{\xi}|)}{|\boldsymbol{\xi}|^2}\xi_i\xi_i\mathrm{d}\boldsymbol{\xi},$$

and we have used the spherical coordinates, $\xi_1 = |\boldsymbol{\xi}|sin\theta cos\phi, \xi_2 = |\boldsymbol{\xi}|sin\theta sin\phi$, and $\xi_3 = |\boldsymbol{\xi}|cos\theta$ where

$$\gamma = \frac{3}{m_1}.$$

Discretization

To solve the non-local equation we have chosen to split the domain into equally spaced nodes with spacing of Δx. The discretized version of our model is presented here.

$$0 = \rho c \frac{T^{n+1}(\mathbf{x}_i) - T^n(\mathbf{x}_i)}{\Delta t} - 2k \sum_j \gamma \frac{\omega(|\boldsymbol{\xi}|)}{|\boldsymbol{\xi}|^2} \left(T^{n+1}(\mathbf{x}_j) - T^{n+1}(\mathbf{x}_i) \right) A_j \tag{30}$$

Above A_j can be thought of as Δx^2 for 2-dimensional case and as Δx for the 1D case. α subscript represents x and y directions. Above $\mathbf{x}_j := \mathbf{x}_i + \boldsymbol{\xi}$ where j stands for a neighboring node and x_i is the spatial position of the node of interest. In this discretized model the local limit is achieved by increasing the number of neighbours while increasing the number of nodes at a faster rate. This ensures that the overall horizon size approaches zero. To achieve the non-local limit one would increase the number of nodes while keeping the horizon size constant.

Investigation on Characteristics of Proposed Non-local Model

Non-local models are built based on a kernel function , ω the shape and size of this kernel usually becomes irrelevant as the local limit is considered. It can however be shown that only the right shape and size for the kernel will result in the correct non-local solution. These correct non-local solutions are typically the results of actual experiments or results of already established models such as MD models or pore network models. Here we will investigating a problem of heat transfer through Cu-Ar nanofuild. This combination is chosen as it results in an easy to setup and accurate MD model. We will then be able to compare the results of our non-local model both with classical models of heat transer and with MD results. Here we will investigate both transient and steady-state problems and report our verdict on the importance of kernel shape and size in each case.

Steady-State Heat Transfer The steady-state condition can be modeled both using the stead-state equations or by allowing the transient solution to reach equilibrium. Two independent non-local models were derived for each case and each model was solved by two different kernels. It must be noted that the kernels are chosen in a way that the area under them would be equal no matter what shape or horizon size. This area is representative of the heat conductivity of the nanofluid and is a physical property of the fluid. Hence this area should always be kept constant when running simulations. For this investigation we will be comparing the kernel presented in fig.15 with a constant line kernel.
The transient model is already presented above. The steady state model derived for this problem is

$$q = -k \sum_j \gamma \omega(|\boldsymbol{\xi}|)(T(\mathbf{x}_j) - T(\mathbf{x}_i)) \frac{\xi_j}{|\boldsymbol{\xi}|^2} \mathrm{A_j}. \tag{31}$$

The result of non-local simulations are presented below. It is shown that as the non-local limit is

approached both models approach the same results. It can also be seen that no matter the kernel shape or size the models give almost identical solutions for steady-state heat conduction with constant heat flux through the nanofluid. This is an important finding which indicates that for steady-state heat conduction problems the shape and size of the non-local kernel does not effect the result of the simulation. In such cases simple kernel shapes such as triangular kernels are recommended as they typically reduce the convergence time [4].

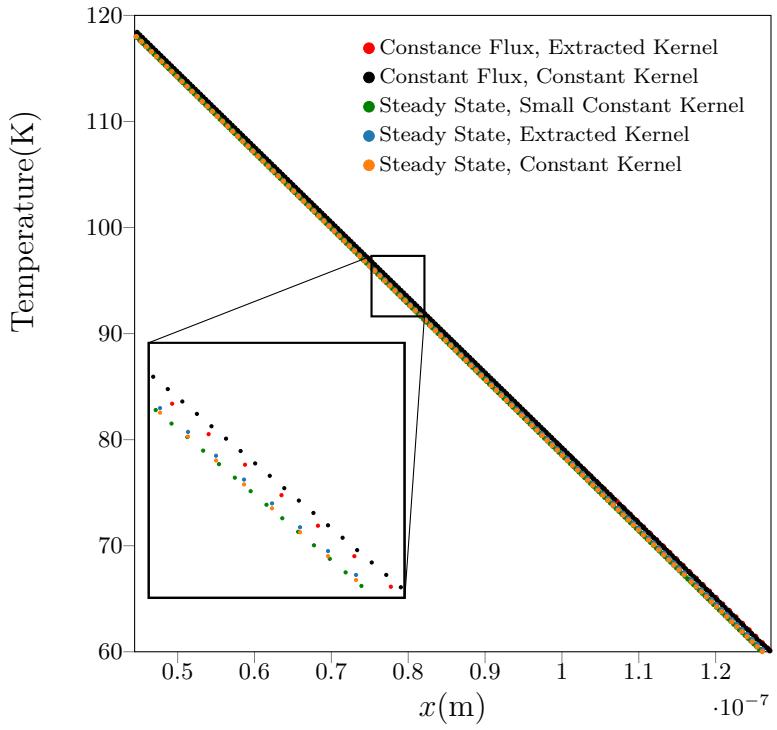

Figure 20: Results of simulations for steady state problem with contant flux boundary conditions

In figure 20 small constant kernel is a kernel that looks like a horizontal line but has a small horizon compared to our extracted kernel.

Transient Heat transfer In transient problems the horizon shape was shown to have a measurable effect on the result of the simulation when the domain size is within an order of magnitude of the horizon. Before moving forward we need to mention the fact that the expected heat conduction enhancment of nanofluids over the base fluid is typically below 10 percent and so a kernel characteristic that can change the final result by a few percents should be considered signicant. But maybe what was even more important was the difference in the results when the horizon size was altered. Temperature results show significant dependence on the chosen horizon size. As a reminder, all these results where achieved while ensuring that the area under the kernel curve equals the value of the heat conductivity measured by MD model. This means that all of these non-local models converge to the same local limits.

This limit is shown in figure 21 in black solid line. It is clear from these results that a significantly different temperature profile should be expected if the horizon size is not chosen correctly.

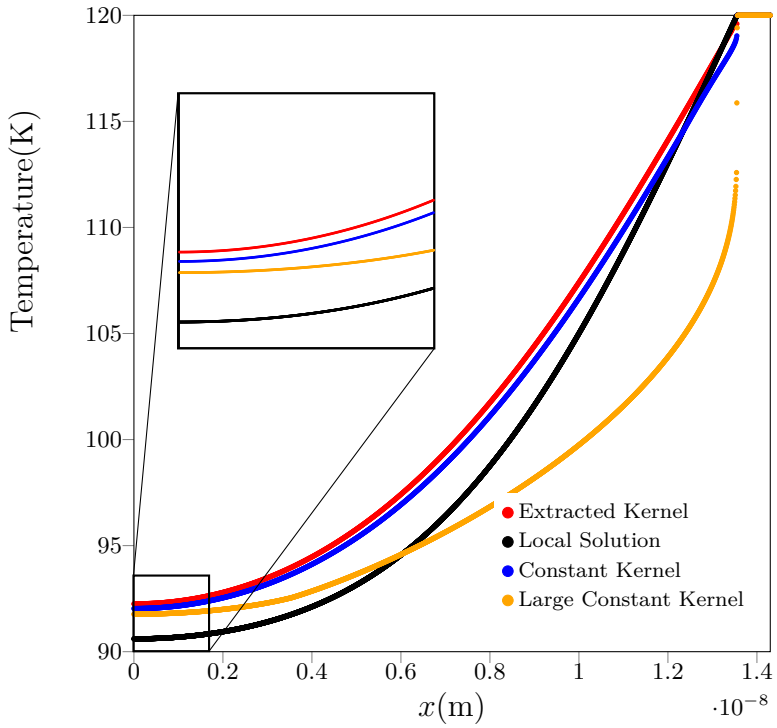

Figure 21: Results of simulations for steady state problem with contant flux boundary conditions

This result confirms what has previously been reported on similar investigations [9]. But what was not clearly mentioned in previous work is that above results are for the case were domain size is within an order of magnitude of the horizon size. It can be shown both mathematically and numerically that as the domain to horizon size ratio is increased, results of all simulations tend to converge to the local limit. In such cases the importance of chosing correct horizon size and shape is reduced. In fact this high ratio would have the physical meaning that the domain is almost perfectly homogeneous and in such cases one could argue that if there are no singularities in the domain then one could simply use a classical model without seeing too much deviation from the true non-local solution. To clarify this idea we ran all the above simulations again but this time in a much larger domain. The result of this large simulation clearly shows the convergence of all results to the local limit.

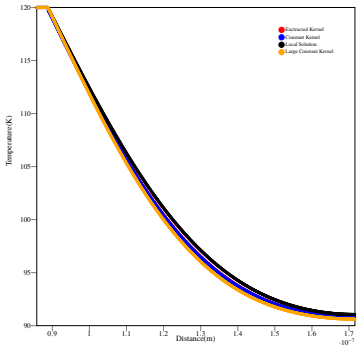

Figure 22: Plot of different simulation for a large domain with constant temperature boundary condition showing the convergence of all results

This is a very interesting result as non-local models are proven to be much more capable than classical local models when any non-homogeneity occurs inside the domain. We have so far shown that if the chosen domain size is large enough compared to the homogeneities in the domain, even a constant kernel results in satisfactory non-local solution.

Now lets focus on a case where the transient nature of the problem becomes strong enough to cause a significant difference in the heat transfer process. This problem can be a simulation of a nanofluid running through the engine of a car. As the nanofluid is circulated through the engine it will periodically get in contact with the hot surface of the engine block and the cold surface of the radiator. Finally to make the simulation even more irregular, the hot and the cold surfaces are assumed to have a sinusoidally varying temperatures.

As expected this simulation showed the highest difference when using the extracted versus using the constant kernel. It should be noted that for this simulation the domain size is chosen to be much higher than the horizon size. The difference in simulation outcome of such unsteady problems would only grow as the domain size gets closer to the horizon cutoff. Attempting to run a MD model on this problems resulted in such high oscillations that no meaningful outcome was achieved. This is another advantage of the proposed non-local model as it is capable of not only running non-equilibrium problems faster but also providing results that have much less noise.

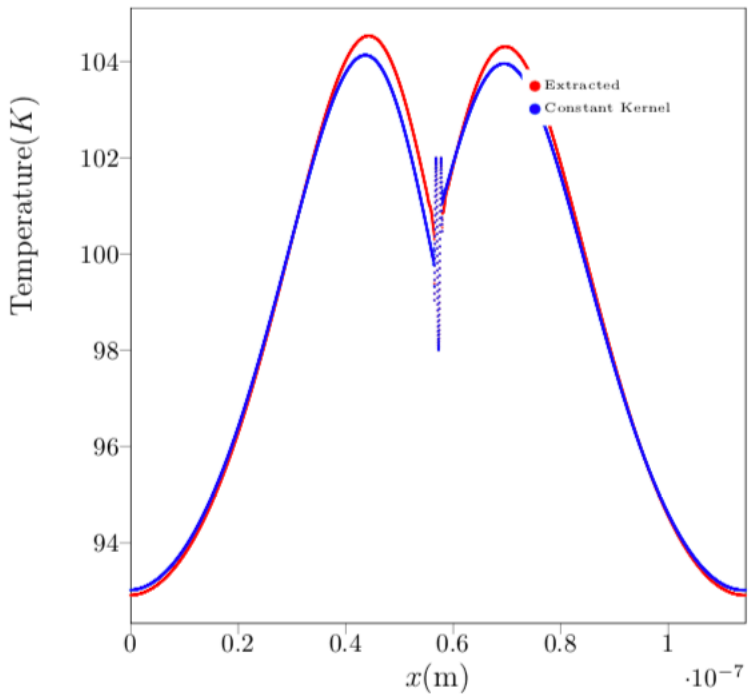
Temperature(K)
104
102
100
98
96
94
0
0.2
0.4
0.6
0.8
1
x(m)
·10−7
Extracted
Constant Kernel

Conclusion

This paper presentated a systematic approach for deriving the non-local kernel for nanofluids. the validity of the approach was tested by predicting heat transfer coefficient of different nanofluids and comparing the result against Green-Kubo and Hamilton-Crosser predictions. The calculated kernels were then used in a heat transfer process to show that the result of a steady-state problem does not depend on the shape or the size of the non-local kernel. It was further shown that the chosen nonlocal kernel can significantly alter the result of a transient simulation given that the domain size is within an order of a magnitude larger than the size of homogeneities in the system. In the considered heat transfer problem, we were interested at taking a close look at the interactions between nano-particles and neighboring Argon and as a result the domain needed to be on the same order of magnitude as the nanoparticle size. Similar cases might happen with solid mechanics field if material behaivior near crack tip is being studied.

Bibliography

[1] Om. P. Agrawal. Fractional variational calculus in terms of Riesz fractional derivatives. *Journal of Physics A: Mathematical and Theoretical*, 40(24):6287, 2007.

[2] Daniel S Banks and Cécile Fradin. Anomalous diffusion of proteins due to molecular crowding. *Biophysical journal*, 89(5):2960–2971, 2005.

[3] PSSK Bhattacharya, SK Saha, A Yadav, PE Phelan, and RS Prasher. Brownian dynamics simulation to determine the effective thermal conductivity of nanofluids. *Journal of Applied Physics*, 95(11):6492–6494, 2004.

[4] Florin Bobaru and Monchai Duangpanya. The peridynamic formulation for transient heat conduction. *International Journal of Heat and Mass Transfer*, 53(19-20):4047–4059, 2010.

[5] Florin Bobaru and Monchai Duangpanya. A peridynamic formulation for transient heat conduction in bodies with evolving discontinuities. *Journal of Computational Physics*, 231(7):2764–2785, 2012.

[6] Florin Bobaru, Mijia Yang, Leonardo Frota Alves, Stewart A Silling, Ebrahim Askari, and Jifeng Xu. Convergence, adaptive refinement, and scaling in 1d peridynamics. *International Journal for Numerical Methods in Engineering*, 77(6):852–877, 2009.

[7] A. Carpinteri, P. Cornetti, and A. Sapora. Nonlocal elasticity: an approach based on fractional calculus. *Meccanica*, 49(11):2551–2569, 2014.

[8] M Chandrasekar and S Suresh. A review on the mechanisms of heat transport in nanofluids. *Heat Transfer Engineering*, 30(14):1136–1150, 2009.

[9] Amir H Delgoshaie, Daniel W Meyer, Patrick Jenny, and Hamdi A Tchelepi. Non-local formulation for multiscale flow in porous media. *Journal of Hydrology*, 531:649–654, 2015.

[10] Qiang Du, Max Gunzburger, Richard B Lehoucq, and Kun Zhou. Analysis and approximation of nonlocal diffusion problems with volume constraints. *SIAM review*, 54(4):667–696, 2012.

[11] Qiang Du, Max Gunzburger, Richard B Lehoucq, and Kun Zhou. A nonlocal vector calculus, nonlocal volume-constrained problems, and nonlocal balance laws. *Mathematical Models and Methods in Applied Sciences*, 23(03):493–540, 2013.

[12] Jeffrey A Eastman, SR Phillpot, SUS Choi, and P Keblinski. Thermal transport in nanofluids. *Annu. Rev. Mater. Res.*, 34:219–246, 2004.

[13] Albert Einstein. *Investigations on the Theory of the Brownian Movement*. Courier Corporation, 1956.

[14] A.C. Eringen. Line crack subject to shear. *International Journal of Fracture*, 14(4):367–379, 1978.

[15] Birendra Jha, Luis Cueto-Felgueroso, and Ruben Juanes. Fluid mixing from viscous fingering. *Physical review letters*, 106(19):194502, 2011.

[16] Hyun Uk Kang, Sung Hyun Kim, and Je Myung Oh. Estimation of thermal conductivity of nanofluid using experimental effective particle volume. *Experimental Heat Transfer*, 19(3):181–191, 2006.

[17] Amit Katiyar, John T Foster, Hisanao Ouchi, and Mukul M Sharma. A peridynamic formulation of pressure driven convective fluid transport in porous media. *Journal of Computational Physics*, 261:209–229, 2014.

[18] Phillbot Keblinski, SR Phillpot, SUS Choi, and JA Eastman. Mechanisms of heat flow in suspensions of nano-sized particles (nanofluids). *International journal of heat and mass transfer*, 45(4):855–863, 2002.

[19] Joseph Klafter and Igor M Sokolov. Anomalous diffusion spreads its wings. *Physics world*, 18(8):29, 2005.

[20] Larry W Lake and Paul B Venuto. A niche for enhanced oil recovery in the 1990s. *Oil & Gas Journal*, 88(17):62–67, 1990.

[21] Ling Li, Yuwen Zhang, Hongbin Ma, and Mo Yang. Molecular dynamics simulation of effect of liquid layering around the nanoparticle on the enhanced thermal conductivity of nanofluids. *Journal of nanoparticle research*, 12(3):811–821, 2010.

[22] Gary A Pope et al. The application of fractional flow theory to enhanced oil recovery. *Society of Petroleum Engineers Journal*, 20(03):191–205, 1980.

[23] Philip Geoffrey Saffman and Geoffrey Taylor. The penetration of a fluid into a porous medium or hele-shaw cell containing a more viscous liquid. In *Proceedings of the Royal Society of London A: Mathematical, Physical and Engineering Sciences*, volume 245, pages 312–329. The Royal Society, 1958.

[24] Suranjan Sarkar and R Panneer Selvam. Molecular dynamics simulation of effective thermal conductivity and study of enhanced thermal transport mechanism in nanofluids. *Journal of applied physics*, 102(7):074302, 2007.

[25] Pablo Seleson, Michael L Parks, Max Gunzburger, and Richard B Lehoucq. Peridynamics as an upscaling of molecular dynamics. *Multiscale Modeling & Simulation*, 8(1):204–227, 2009.

[26] S.A. Silling and E. Askari. A meshfree method based on the peridynamic model of solid mechanics. *Computers and Structures*, 83(17-18):1526–1535, 2005.

[27] Stewart A Silling. Reformulation of elasticity theory for discontinuities and long-range forces. *Journal of the Mechanics and Physics of Solids*, 48(1):175–209, 2000.

[28] KH Solangi, SN Kazi, MR Luhur, A Badarudin, A Amiri, Rad Sadri, MNM Zubir, Samira Gharehkhani, and KH Teng. A comprehensive review of thermo-physical properties and convective heat transfer to nanofluids. *Energy*, 89:1065–1086, 2015.

[29] GM Viswanathan, EP Raposo, and MGE Da Luz. Lévy flights and superdiffusion in the context of biological encounters and random searches. *Physics of Life Reviews*, 5(3):133–150, 2008.

[30] Xiang-Qi Wang and Arun S Mujumdar. Heat transfer characteristics of nanofluids: a review. *International journal of thermal sciences*, 46(1):1–19, 2007.

[31] Matthias Weiss, Hitoshi Hashimoto, and Tommy Nilsson. Anomalous protein diffusion in living cells as seen by fluorescence correlation spectroscopy. *Biophysical journal*, 84(6):4043–4052, 2003.

[32] W Yu and SUS Choi. The role of interfacial layers in the enhanced thermal conductivity of nanofluids: a renovated maxwell model. *Journal of nanoparticle research*, 5(1-2):167–171, 2003.